The Astrophysical Journal, 963:107 (18pp), 2024 March 10 https://doi.org/10.3847/1538-4357/ad167f
© 2024. The Author(s). Published by the American Astronomical Society.
OPEN ACCESS

Multispacecraft Observations of a Widespread Solar Energetic Particle Event on 2022 February 15–16

L. Y. Khoo[1], B. Sánchez-Cano[2], C. O. Lee[3], L. Rodríguez-García[4,5], A. Kouloumvakos[6], E. Palmerio[7], F. Carcaboso[8], D. Lario[9], N. Dresing[10], C. M. S. Cohen[11], D. J. McComas[1], B. J. Lynch[3], F. Fraschetti[12,13], I. C. Jebaraj[10], J. G. Mitchell[9], T. Nieves-Chinchilla[9], V. Krupar[9,14], D. Pacheco[15], J. Giacalone[12], H.-U. Auster[16], J. Benkhoff[17], X. Bonnin[18], E. R. Christian[9], B. Ehresmann[19], A. Fedeli[10], D. Fischer[20], D. Heyner[16], M. Holmström[21], R. A. Leske[11], M. Maksimovic[18], J. Z. D. Mieth[16], P. Oleynik[10], M. Pinto[17], I. Richter[16], J. Rodríguez-Pacheco[4], N. A. Schwadron[1,22], D. Schmid[20], D. Telloni[23], A. Vecchio[18,24], and M. E. Wiedenbeck[25]

[1] Department of Astrophysical Sciences, Princeton University, Princeton, NJ 08544, USA; lykhoo@princeton.edu
[2] School of Physics and Astronomy, University of Leicester, LE1 7RH Leicester, UK
[3] Space Sciences Laboratory, University of California, Berkeley, CA 94720, USA
[4] Universidad de Alcalá, Space Research Group (SRG-UAH), E-28801 Alcalá de Henares, Madrid, Spain
[5] European Space Agency (ESA), European Space Astronomy Centre (ESAC), Camino Bajo del Castillo s/n, E-28692 Villanueva de la Cañada, Madrid, Spain
[6] The Johns Hopkins University Applied Physics Laboratory, Laurel, MD 20723, USA
[7] Predictive Science Inc., San Diego, CA 92121, USA
[8] Postdoctoral Program Fellow, NASA Goddard Space Flight Center, Greenbelt, MD 20771, USA
[9] Heliophysics Science Division, NASA Goddard Space Flight Center, Greenbelt, MD 20771, USA
[10] Department of Physics and Astronomy, University of Turku, FI-20014 Turku, Finland
[11] California Institute of Technology, Pasadena, CA 91125, USA
[12] Department of Planetary Sciences, Lunar and Planetary Lab, Tucson, AZ 85721, USA
[13] Center for Astrophysics, Harvard & Smithsonian, Cambridge, MA 02138, USA
[14] Goddard Planetary Heliophysics Institute, University of Maryland, Baltimore, MD 21250, USA
[15] Deep Space Exploration Laboratory/School of Earth and Space Sciences, University of Science and Technology of China, Hefei 230026, China
[16] Institut für Geophysik und extraterrestrische Physik, TU Braunschweig, D-38106 Braunschweig, Germany
[17] European Space Research and Technology Centre, European Space Agency, 2201 AZ Noordwijk, The Netherlands
[18] LESIA, Observatoire de Paris, Université PSL, CNRS, Sorbonne Université, Université de Paris, F-92195 Meudon, France
[19] Solar System Science and Exploration Division, Southwest Research Institute, Boulder, CO 80302, USA
[20] Space Research Institute, Austrian Academy of Sciences, A-8042 Graz, Austria
[21] Swedish Institute of Space Physics, SE-98192 Kiruna, Sweden
[22] Space Science Center, University of New Hampshire, Durham, NH 03824, USA
[23] National Institute for Astrophysics, Astrophysical Observatory of Torino, I-10025 Pino Torinese, Italy
[24] Radboud Radio Lab, Department of Astrophysics, Radboud University, 6525 AJ Nijmegen, The Netherlands
[25] Jet Propulsion Laboratory, Pasadena, CA 91011, USA
Received 2023 October 31; revised 2023 December 11; accepted 2023 December 15; published 2024 March 5

Abstract

On 2022 February 15–16, multiple spacecraft measured one of the most intense solar energetic particle (SEP) events observed so far in Solar Cycle 25. This study provides an overview of interesting observations made by multiple spacecraft during this event. Parker Solar Probe (PSP) and BepiColombo were close to each other at 0.34–0.37 au (a radial separation of ∼0.03 au) as they were impacted by the flank of the associated coronal mass ejection (CME). At about 100° in the retrograde direction and 1.5 au away from the Sun, the radiation detector on board the Curiosity surface rover observed the largest ground-level enhancement on Mars since surface measurements began. At intermediate distances (0.7–1.0 au), the presence of stream interaction regions (SIRs) during the SEP arrival time provides additional complexities regarding the analysis of the distinct contributions of CME-driven versus SIR-driven events in observations by spacecraft such as Solar Orbiter and STEREO-A, and by near-Earth spacecraft like ACE, SOHO, and WIND. The proximity of PSP and BepiColombo also enables us to directly compare their measurements and perform cross-calibration for the energetic particle instruments on board the two spacecraft. Our analysis indicates that energetic proton measurements from BepiColombo and PSP are in reasonable agreement with each other to within a factor of ∼1.35. Finally, this study introduces the various ongoing efforts that will collectively improve our understanding of this impactful, widespread SEP event.

Unified Astronomy Thesaurus concepts: Solar energetic particles (1491); Heliosphere (711); Solar coronal mass ejections (310)

1. Introduction

The study of the spatial distribution of solar energetic particles (SEPs), as well as their intensity variation as a function of time, energies, and species, in the inner heliosphere is fundamental to understanding the mechanism(s) behind particle acceleration and transport (e.g., Dresing et al. 2012; Reames et al. 2013; Lario et al. 2014; Kouloumvakos et al.

Original content from this work may be used under the terms of the Creative Commons Attribution 4.0 licence. Any further distribution of this work must maintain attribution to the author(s) and the title of the work, journal citation and DOI.

2015; Cohen et al. 2017; Xie et al. 2019; Rodríguez-García et al. 2021; Sanchez-Cano et al. 2023). Various mechanisms have been proposed to explain observations of so-called widespread SEP events, which are characterized by a longitudinal separation of at least 80° between the eruption's source region and the spacecraft's magnetic footpoint for the most widely separated spacecraft observing the event (Dresing et al. 2014). Particle acceleration by coronal mass ejection (CME)-driven shocks is one of the favored mechanisms to interpret such widespread events (e.g., Cane et al. 1988; Reames et al. 1996; Lario et al. 2016). It offers a straightforward explanation of how particles can access a wide interplanetary region in a short time, as the shock itself can have a large longitudinal extent. However, studies such as Richardson & Cane (1993), Cane (1996), and de Lucas et al. (2011) have pointed out significant discrepancies between the size of the interplanetary shock inferred from in situ observations and the size of the shock required to account for the longitudinal spread of SEPs, casting doubts on the feasibility of this mechanism alone to generate all widespread SEPs. Other studies suggest that these widespread SEP events could be caused by additional mechanisms such as cross-field particle diffusion within the interplanetary medium (e.g., Wibberenz & Cane 2006; Lario et al. 2017), the meandering of magnetic field lines due to plasma turbulence (e.g., Giacalone & Jokipii 2012; Laitinen et al. 2015), the injection of particles over broad regions close to the Sun (Gómez-Herrero et al. 2015; Dresing et al. 2023), and the presence of preceding large-scale transients in the heliosphere (e.g., Richardson & Cane 1996; Palmerio et al. 2021). In all these scenarios, particles can effectively propagate across the interplanetary magnetic field and lead to a wide spread of particles across the heliosphere.

Multi-spacecraft measurements are critical to the characterization of SEP variations in the heliosphere. A major improvement in longitudinal coverage of the available SEP measurements came with the launch of the twin Solar Terrestrial Relations Observatory (STEREO; Kaiser et al. 2008) spacecraft, which allowed detection and analysis of myriad multipoint SEP events at 1 au (e.g., Richardson et al. 2014). The launch of more recent heliophysics missions such as the Parker Solar Probe (PSP; Fox et al. 2016) and Solar Orbiter (Müller et al. 2020), as well as planetary missions in near-continuous operation during their cruise phase such as BepiColombo (Benkhoff et al. 2021), marks a new era in heliophysics research. The wide radial and longitudinal coverage of these multi-spacecraft observations provides us with improved remote-sensing and in situ capabilities to achieve a better understanding of the spatial variation and the source of SEP events. The first widespread SEP event of Solar Cycle 25 occurred on 2020 November 29 and was observed at five widely separated locations (over 230° in longitude) in the inner ($\leqslant$1.5 au) heliosphere (e.g., Cohen et al. 2021; Kollhoff et al. 2021; Kouloumvakos et al. 2022a; Palmerio et al. 2022). By combining remote-sensing observations and in situ measurements, Kolhoff et al. (2021) provided a comprehensive analysis of the widespread SEP event. Their study also demonstrated that it is challenging to reconcile measurements from multiple spacecraft and pinpoint the underlying particle source and transport mechanism that leads to such a widespread SEP event. For the same event, Kouloumvakos et al. (2022a) demonstrated that a prominent increase in SEPs was recorded by even the farthest observers, such as Earth, despite the magnetic connection to these observers involved only a non-shocked compression wave. Their findings suggest that perpendicular diffusion, together with the initial very wide shock extension, may account for the widespread characteristics of this event. Furthermore, Dresing et al. (2023) reported the second widespread SEP event of Solar Cycle 25, which happened on 2021 April 17 and was observed by five well-separated spacecraft over a longitudinal spread of ∼210°. Their detailed analysis suggests that the proton event was likely caused by the CME-driven shock, while the electron event was dominated by a flare-related source.

On 2022 February 15, several spacecraft in the inner heliosphere (within Mar's orbit) observed a large solar eruption around 22:00 UT from the far side of the Sun with respect to Earth as shown in Figure 1. This solar eruption led to a fast CME and the third reported widespread SEP event that was observed by multiple spacecraft since the start of Solar Cycle 25. Spacecraft that measured SEP enhancements during this event period include PSP, BepiColombo, STEREO-A, Solar Orbiter, near-Earth assets, such as the Solar and Heliospheric Observatory (SOHO; Domingo et al. 1995), the Advanced Composition Explorer (ACE; Stone et al. 1998), and the Global Geospace Science Wind satellite (Wind; Ogilvie & Desch 1997), as well as spacecraft at Mars, such as the Mars Atmosphere and Volatile Evolution mission (MAVEN; Jakosky et al. 2015), Mars Express (MEX; Chicarro et al. 2004), and the Mars Science Laboratory (MSL; Grotzinger et al. 2012; see the left panel of Figure 1 for the configuration of the available observers). This event also represents the first time that a prominence eruption was observed at extreme ultraviolet (EUV) wavelengths (in the 304 Å channel) above 6 $R_\odot$ (by Solar Orbiter as shown in Mierla et al. 2022).

This SEP event constitutes one of the first opportunities to directly compare measurements between BepiColombo and PSP, as both spacecraft were nearly colocated during this event. The fortuitous spacecraft configuration also enables us to study the propagation of an intense SEP event in the inner heliosphere with mission observations over a wide longitudinal range. During this event, MSL also observed the largest ground-level enhancement event on Mars since its operation. Given the large scope of such a widespread SEP event, this study aims to provide a summary of the SEP observation made by multiple spacecraft with an emphasis on measurements made by PSP, BepiColombo (and their cross-calibration of particle observation), and different missions at Mars, as well as highlighting the unique observations associated with this event. As several more studies are currently underway to examine various details of this widespread SEP event, this article also serves as a guide and overview for those upcoming investigations.

Section 2 provides a list of the instrumentation employed in this study. Section 3 shows an overview of the 2022 February 15 eruption, including an overview of the solar activity and the corresponding spacecraft locations during this event. Section 4 presents multi-spacecraft observations of the event with a focus on the particle measurement comparison between BepiColombo and PSP as well as energetic particle observations at Mars. Finally, our findings are summarized in Section 5.

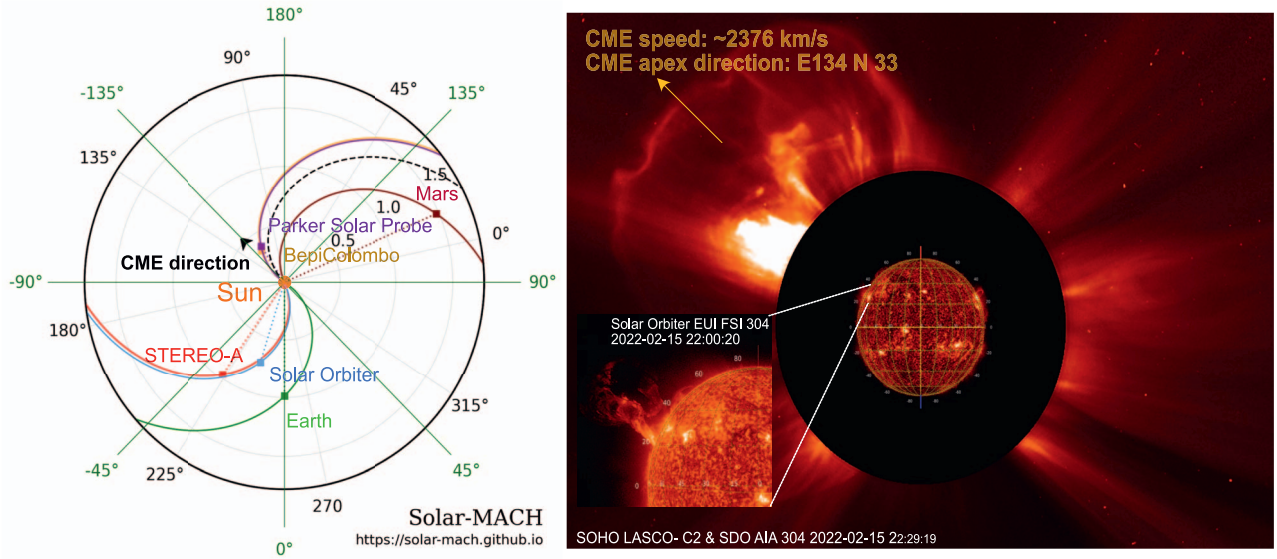

Figure 1. Overview of the spacecraft and planet configuration as well as solar activity on 2022 February 15. Left panel: Spacecraft and planet configuration in the inner solar system during the 2022 February 15 event, including BepiColombo, PSP, Mars, Earth, STEREO-A, and Solar Orbiter. The orbit plot is created with the Solar Solar MAgnetic Connection HAUS (Solar-MACH; Gieseler et al. 2023) tool. Right panel: Overview of the solar activity on 2022 February 15, composed of images from SDO/AIA 304 Å and SOHO LASCO-C2 around 22:30 UT using JHelioviewer (Müller et al. 2017). It provides an overview of the corresponding CME from the erupting filament around 22:00 UT on 2022 February 15. The bottom left insert provides a better view of the erupting filament from the perspective of Solar Orbiter EUI FSI 304 Å. Based on the graduated cylinder shell (GCS; Thernisien et al. 2006, 2009) 3D model, the CME apex was heading in the direction E134 N33 with a speed of $\sim$2376 km s^{-1}.

2. Data Set

In this section, we provide a summary of the main data sets used in this analysis. Spacecraft are introduced according to their radial distance from the Sun during this event, starting from the closest.

BepiColombo. BepiColombo is a joint mission between the European and Japanese space agencies. In this study, we used data from the Mercury Planetary Orbiter (MPO), the European module part of the mission. Currently, BepiColombo is in its cruise phase to Mercury. This mission was launched in 2018 October and will arrive at Mercury in 2025 December. During its cruise phase, the different modules of BepiColombo are traveling in a stacked configuration, with some instruments in operation (Hadid et al. 2021; Mangano et al. 2021). We used the two instruments that were operating during this event: the MPO magnetometer (MPO-MAG; Heyner et al. 2021), which is formed by two triaxial fluxgate magnetometers mounted on a boom and separated by 2.9 m, and the MPO BepiColombo Environment Radiation Monitor (BERM; Pinto et al. 2022), which is a particle detector that can measure electrons (0.15–10 MeV), protons (1.5–100 MeV), and heavy ions (1–50 MeV·mg^{-1}·cm^{-2}). Proton channels from MPO/BERM are provided in flux units, while the electron channels are provided in counts, as the team is currently working on the calibration of these channels. BERM is generally pointing antisunward during the cruise period. To gain the right trajectory to reach Mercury, BepiColombo regularly performs several solar electric propulsion maneuvers (Montagnon et al. 2021), one of which occurred during the 2022 February 15 event. We note that BERM observations were not affected by this maneuver, and the MPO-MAG data had been specially treated to remove the additional noise that the maneuver introduced (see more details in Palmerio et al., this issue). No other instruments were in operation during this solar event, due to this technical maneuver.

Parker Solar Probe (PSP). PSP was launched in 2018 with the goals of understanding what heats the solar corona, accelerates the solar wind, and energizes and transports SEPs. It is in a heliocentric orbit with an inclination of about 3.4° and an orbital period of $\sim$3 months. This study utilized measurements from the fluxgate magnetometer part of the FIELDS (Bale et al. 2016) experiment that provides direct measurements of electric and magnetic fields and waves, the Integrated Science Investigation of the Sun (IS⊙IS, McComas et al. 2016) that measures energetic particles ranging from 10 s of keV to 100 s of MeV, and the Solar Wind Electrons Alphas and Protons (SWEAP; Kasper et al. 2016) suite that measures solar wind particles and their properties such as temperature, velocity, and density. The IS⊙IS instrument suite consists of two Energetic Particle Instruments that measure lower-energy (EPI-Lo) and higher-energy (EPI-Hi) particles. EPI-Lo is a time-of-flight mass spectrometer that covers nearly a complete hemisphere using 80 apertures, while EPI-Hi consists of three solid-state detector telescopes that cover five large field-of-view apertures. During this event period, the spacecraft performed multiple rolls as the spacecraft approached the perihelion. We note that the IS⊙IS data were not affected by this activity, and higher-level data products like EPI-lo L3 pitch angle data have taken the changes in the instrument's viewing direction into account.

Solar Orbiter. Launched in 2020 February, Solar Orbiter is also a heliocentric orbit mission with an eventual higher inclination to the ecliptic plane (reaching $\sim$24° over the primary mission and $\sim$33° during the proposed extended mission phase; it was at $-3\overset{\circ}{.}1$ Carrington latitude during this event) and an orbital period of 168 days. This study used data from the Energetic Particle Detector (EPD; Rodríguez-Pacheco et al. 2020), an instrument suite that provides energetic particle data in a range from a few keV to 100 MeV. In addition, we obtained electric and magnetic field measurements from the magnetometer (MAG; Horbury et al. 2020) and Radio and

Plasma Waves (RPW; Maksimovic et al. 2020) instruments. Data from the Solar Wind Plasma Analyzer (SWA; Owen et al. 2020) provide the in situ solar wind measurements. This study also used remote-sensing EUV measurements from the Full Sun Imager (FSI) part of the Extreme Ultraviolet Imager (EUI; Rochus et al. 2020) telescope.

STEREO-A. THE STEREO mission consisted of two almost identical spacecraft: one was launched at an orbit just inside 1 au ("Ahead", also known as STEREO-A) and one outside the Earth's orbit ("Behind", also known as STEREO-B, which ceased operations in 2014). This study analyzed remote-sensing imagery as well as in situ solar wind, energetic particles, and magnetic field measurements from instrument suites such as In situ Measurements of Particles and CME Transients (IMPACT; Luhmann et al. 2008), PLasma and SupraThermal Ion Composition (PLASTIC; Galvin et al. 2008), the Sun Earth Connection Coronal and Heliospheric Investigation (SECCHI; Howard et al. 2008), and STEREO/WAVES (S-WAVES; Bougeret et al. 2008). Specifically, we studied 100s keV to a few MeV protons from the IMPACT instrument suite.

Earth. This study used remote-sensing and in situ measurements from near-Earth spacecraft such as SOHO, Wind, ACE, and the Solar Dynamics Observatory (SDO; Pesnell et al. 2012). SOHO, Wind, and ACE orbit the Sun at the Sun–Earth Lagrange L1 point, while SDO is on a geosynchronous orbit. This study used EUV images from the Atmospheric Imaging Assembly (AIA; Lemen et al. 2012) on board SDO and white-light data from the Large Angle Spectroscopic Coronagraph (LASCO; Brueckner et al. 1995) on board SOHO to understand the solar source and early evolution of this event. In addition, we analyzed energetic particle measurements from the Energetic and Relativistic Nuclei and Electron (ERNE; Torsti et al. 1995, 13–140 MeV protons) telescope as well as the Electron Proton Helium Instrument (EPHIN) part of the Comprehensive Suprathermal and Energetic Particle Analyser (COSTEP; Müller-Mellin et al. 1995, 4–53 MeV protons) suite on board SOHO, the 3D Plasma Analyzer (3DP; Lin et al. 1995, 70 keV–6.8 MeV protons) on board the Wind satellite, and the Electron, Proton, and Alpha Monitor (SWEPAM; Gold et al. 1998; 50–4750 keV protons) on board ACE to understand the particle dynamics in the near-Earth environment. We also utilized magnetic field and solar wind measurements as extracted from the Wind Magnetic Field Investigation (MFI; Lepping et al. 1995) and Solar Wind Experiment (SWE; Ogilvie et al. 1995) on board Wind to improve our interpretation of the particle time–intensity profile by investigating the corresponding heliospheric context.

Mars. To investigate the in situ particle dynamics at Mars, this study used measurements from the MAVEN and MEX spacecraft and the MSL Curiosity Rover. Energetic particle fluxes from 20 to 200 keV electrons and 20 keV to 6 MeV protons were obtained from the Solar Energetic Particle (hereafter MAVEN/SEP; Larson et al. 2015) instrument on board the MAVEN spacecraft. To provide context to the SEP observations, we also used solar wind moments from the Analyzer of Space Plasmas and Energetic Atoms (ASPERA-3; Barabash et al. 2006) instrument on board MEX. In addition, we utilized penetrating particle count rate data sets from MAVEN/SEP and the MEX ASPERA-3 Ion Mass Analyzer (IMA) instrument that are caused by electrons with energies >1 MeV and protons >20 MeV that penetrate the internal structure of the instrument (e.g., Ramstad et al. 2018; Futaana et al. 2022). At the Martian surface, the MSL Radiation Assessment Detector (RAD; Hassler et al. 2012) measures the radiation dose that reaches the Gale crater near the equator. Enhancements above the background dose rates are measured when >150 MeV protons penetrate the Martian atmosphere to reach the surface (Guo et al. 2019).

3. Solar Eruptions and the Corresponding Spacecraft Location

This section provides details of the solar eruptions that are relevant to the 2022 February 15–16 SEP event as well as the location of the different spacecraft during this event.

3.1. Overview of the Solar Observations

This large-scale solar eruption during Carrington Rotation 2267 marks one of the most intense solar activities during the present solar cycle. The eruption started around 21:50 UT on 2022 February 15 and was observed at several EUV channels by multiple spacecraft such as STEREO-A, Solar Orbiter, and SDO. From Earth's viewpoint, the eruption occurred behind the east limb of the Sun, suggesting that it was likely associated with the old sunspot region 2936–2938 from the previous Carrington rotation (see Mierla et al. 2022, for a more detailed discussion). These authors showed that the eruption involved a bright prominence, along with three different cores. The last trailing prominence was observed around 01:40 UT on 16 February and was seen at heights as large as 6.6 $R_\odot$, which is near the outer limit of the field of view of the EUI/FSI imager on Solar Orbiter at the time of this event. This makes it the most distant filament observed at EUV wavelengths (Mierla et al. 2022).

Based on 3D fitting results using the Graduated Cylindrical Shell (GCS; Thernisien et al. 2009) model, this CME has an estimated peak speed as high as 2376 km s^{-1} ($\pm$166 km s^{-1}, which is $\pm$7% of the estimated speed; Kwon et al. 2014) and a CME-driven shock speed of $\sim$2315 km s^{-1} ($\pm$185 km s^{-1}, which is $\pm$8% of the determined value; Kwon et al. 2014) at a heliocentric height of 25 $R_\odot$. As seen in Figure A1, the extension of the shock was remarkably broad, reaching coronal regions with an angular separation from the active region of more than 120°. The longitude and latitude of the CME apex were at $-134°$ and 33° in Stonyhurst coordinates (Thompson 2006) with a fixed tilt angle of $-50°$ and a total angular width of $\sim$58° in the ecliptic plane (more details in Appendix A.1). These values are consistent with those reported in Mierla et al. (2022). Based on the CME trajectory and tilt angle resulting from GCS fitting and assuming that the CME did not experience any drastic deflection in interplanetary space, the near-equatorial spacecraft would likely miss the CME nose and encounter the CME southern flank instead.

3.2. Spacecraft Locations during This Event

The SEP event was observed by a fortuitous spacecraft configuration (Figure 1) in the inner heliosphere. Table 1 summarizes the location of different spacecraft during the onset of this event, 22:00 UT on 2022 February 15, including their radial distances, Carrington longitudes, Carrington latitudes, and magnetic footpoints in Carrington longitude, as well as the connection angle, which is defined as the longitudinal separation between the eruption center and the magnetic

Table 1
Location of the Spacecraft and Planets at 22:00 UT on 2022 February 15

Spacecraft	Distance (au)	Spacecraft Carrington Latitude (deg)	Spacecraft Carrington Longitude (deg)	Magnetic Footpoint Carrington Longitude (deg)	Connection Angle[a] (deg)
BepiColombo	0.35	2	115	136	12
PSP	0.38	4	111	135	11
Solar Orbiter	0.72	−3	241	286	162
STEREO-A	0.97	−5	223	284	160
Earth	0.99	−7	258	319	−165
Mars	1.48	0	11	104	−20
Estimated Eruption Source	⋯	33	124	124	0

Note.
[a] The connection angle refers to the longitudinal separation angle between the eruption center and the magnetic footpoint of the spacecraft/planet.

footpoint of the spacecraft, based on a nominal Parker spiral (e.g., Xie et al. 2019; Rodríguez-García et al. 2023). These values are obtained using an open-source tool called Solar Magnetic Connection HAUS (Solar-MACH; Gieseler et al. 2023). It should be noted that the magnetic footpoints assume connection along a nominal Parker Spiral.

BepiColombo was located at ∼0.35 au, making it the closest to the Sun among all spacecraft on 2022 February 15. During this event, BepiColombo was at a Carrington longitude of ∼115° and a latitude of ∼2°. Separated by ∼0.03 au radially, ∼4° in longitude, and ∼2° in latitude away from BepiColombo was PSP, located at ∼0.38 au from the Sun at a Carrington longitude of ∼111° and latitude of ∼4°, and heading toward its perihelion during the event. The magnetic footpoints of both spacecraft were close to the eruption center (connection angles of ∼12° for BepiColombo and ∼11° for PSP).

At ∼0.72 au away from the Sun, Solar Orbiter was at a Carrington longitude of ∼241° and a latitude of ∼-3°. Not far away from Solar Orbiter was the STEREO-A spacecraft, which was located at a Carrington longitude of 223° and Carrington latitude of ∼−5° but radially further away, at ∼0.97 au away from the Sun. The magnetic footpoint of STEREO-A was close to that of Solar Orbiter, but both spacecraft have large longitudinal separation angles (∼160°) between their magnetic footpoints and the eruption center.

During this event, Earth was at a Carrington longitude of ∼258° and a Carrington latitude of ∼−7°, which means the event occurred at the far east limb, from the Earth's perspective, as discussed in Section 2.1. Finally, Mars was located at a heliocentric distance of 1.48 au, a Carrington longitude of ∼11°, and a Carrington latitude of ∼0°. It was also magnetically close to the eruption center, given its small connection angle (∼20°) to the eruption center.

The available spacecraft observations cover a longitudinal range of about 247° and a radial range of about 1.13 au, as shown in Table 1. The largest connection angle to the eruption site is ∼165° (for Earth).

4. Multi-spacecraft Observations

This section provides an overview of in situ measurements and remote-sensing observations from PSP, BepiColombo, Solar Orbiter, STEREO-A, near-Earth observers (SOHO, Wind, and ACE), and Mars (MAVEN, MEX, and MSL).

4.1. SEP Events from a Multi-spacecraft Perspective

Figure 2 provides an overview of the particle, magnetic field, and solar wind dynamics from multiple spacecraft across a longitude range of ∼247° and a connection angle to the eruption center ranging from ∼11° to ∼165°.

As demonstrated in the central panel (a), spacecraft such as MAVEN, BepiColombo, and PSP experienced a more intense particle enhancement compared to observations made by Solar Orbiter, STEREO-A, and Wind. In particular, PSP and BepiColombo captured a relatively similar particle time–intensity profile (Figures 2(b) and (c)). For instance, ∼2.6 MeV protons measured by PSP and BepiColombo showed a clear increase in flux before the shock arrival was followed by a steady decrease. We note that the shock arrived at BepiColombo and PSP around ∼06:30 and ∼07:30 UT, respectively, on 2022 February 16. It was characterized by a sharp jump in magnetic field, solar wind density, and velocity (see Section 4.2 and Palmerio et al. (submitted to the same issue) for more information). As shown in Figure 2(a), the peak flux enhancement is also comparable in magnitude (more discussion in Section 4.2).

Solar Orbiter observed an increase in 2.5 and 17 MeV proton flux around ∼13:00 UT on 2022 February 16 (Figure 2(e)). The proton flux enhancement reached its peak around 02:00 UT on 2022 February 17, approximately one day after the peak of proton enhancements observed by PSP and BepiColombo. The proton flux enhancement was seen up to 80 MeV (not shown) with velocity dispersion, and it coincided with a rise in the solar wind velocity from ∼400 to ∼600 km s^{-1}. A high-speed stream impacted the spacecraft around ∼12:00 UT on February 17. On February 19, Solar Orbiter observed another increase in proton fluxes, up to a few MeV. This flux increase was observed during a period of relatively stable solar wind density and velocity.

With its magnetic footpoint close to that of Solar Orbiter, STEREO-A also observed a flux increase in energetic protons, up to ∼60 MeV, starting on late February 16. These energetic protons experienced a more intense, sudden flux enhancement around ∼19:00 UT on February 17, which was approximately 17 hr after the peak flux enhancement observed by Solar Orbiter. It also observed a second enhancement that was more gradual and peaked on February 19. The first proton enhancement was associated with a shock-like structure in a magnetic field, while the more gradual, second proton enhancement occurred when the solar wind velocity gradually

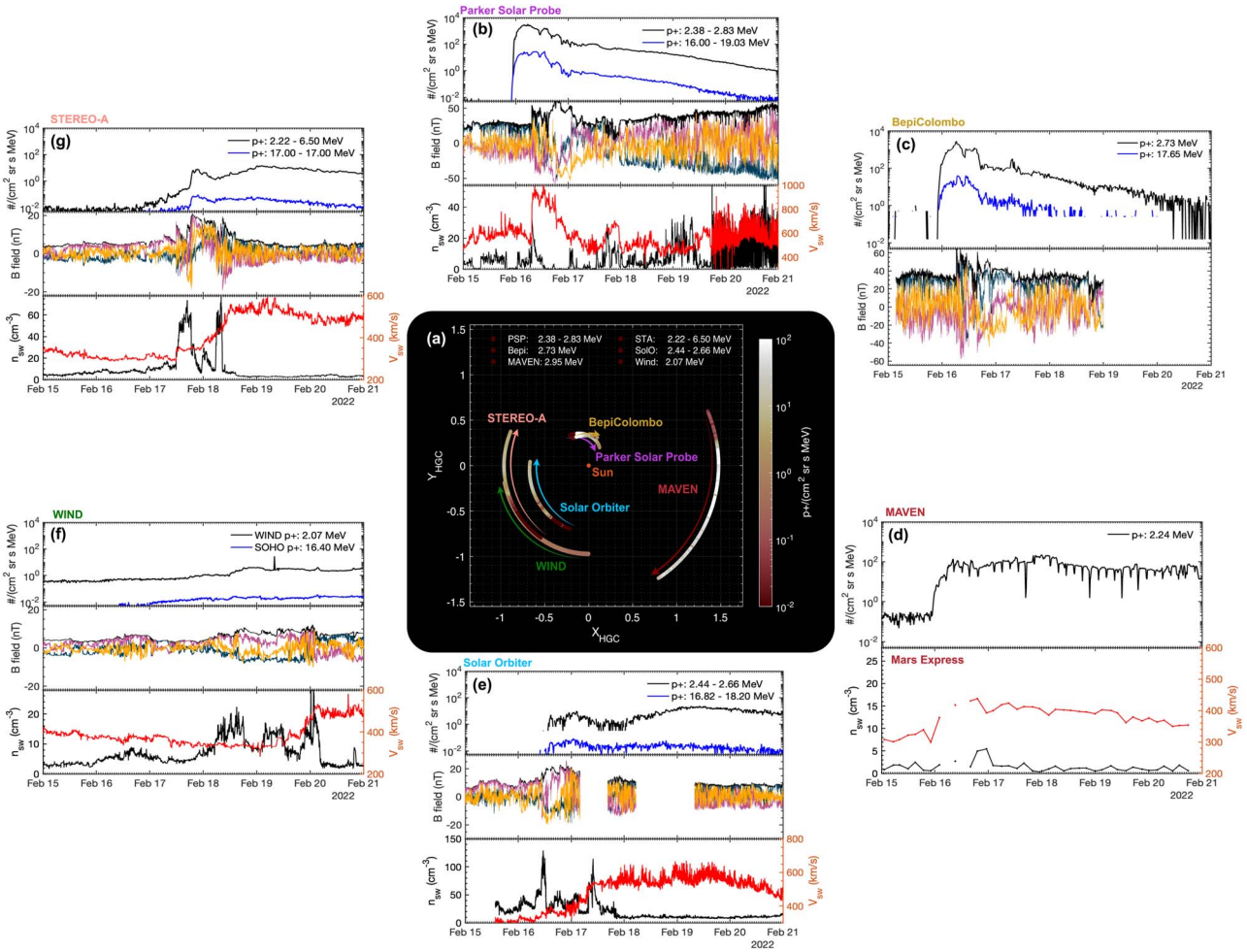

Figure 2. Overview of particle, magnetic field, and solar wind dynamics from a multi-spacecraft perspective. (a) Location of spacecraft in heliographic Carrington coordinates, where the color bar indicates the intensity variation of ∼2 MeV protons observed by (b) PSP, (c) BepiColombo, (d) MAVEN/Mars Express, (e) Solar Orbiter, (f) Wind, and (g) STEREO-A (in the clockwise order) between 2022 February 15 and 21. We note that the WIND data are plotted with a slightly larger marker size to distinguish them from the STEREO-A data. The subplots show ∼2 and ∼17 MeV (when available) proton intensities from different spacecraft as well as measurements of magnetic field, solar wind velocity, and solar wind density when available. We note that proton fluxes from all spacecraft are in a time resolution of 15 minutes, and for (a), only points at every hour (or every fourth point) are plotted in order to reduce overlapping points.

transitioned from lower to higher speed and peaked inside the high-speed stream.

At 1 au, Wind observed 2.07 and 19 MeV proton fluxes that were comparable to those observed by Solar Orbiter and STEREO-A; it measured a small and gradual initial proton event starting on 2022 February 16 that was followed by a relatively larger proton enhancement (up to ∼6 MeV with a clear velocity dispersion) that started around ∼11:00 UT on 2022 February 18 and peaked around ∼22:00 UT the same day. The initial enhancement of proton flux was associated with a rather stable magnetic field with a gradual change in solar wind density, while the latter coincided with a gradual increase in total magnetic field and a relatively high solar wind density. Both enhancements happened in the slow solar wind region.

At 1.5 au, MAVEN identified a flux increase of 2.24 MeV protons on 2022 February 16, which was followed by what appeared to be a minor flux suppression between 18:00 UT on February 16 and 20:00 UT on February 17. The flux increased again around 20:00 UT on February 17 before decaying away starting from 07:00 UT on February 18. The occasional dropout of the proton flux in Figure 2(d) is a result of the MAVEN orbital effect. In Figure 2(d), solar wind moments measurements from the MEX spacecraft show simultaneous increases in the solar wind speed and density during the early hours of 2022 February 16, with peak speed and density occurring toward the end of the day (additional upstream solar wind and IMF observations were not available from MAVEN during this time, due to its orbit geometry). The initial proton enhancement on February 16 appeared to be associated with the increase in solar wind speed and density (see Section 4.3 for more details on the time–intensity variation of the energetic protons at Mars).

The WSA–ENLIL model described in Appendix C illustrates a complex interplanetary condition where the arrival of the high-speed streams complicates the interpretation, making it challenging to discern the influence of the CME and high-speed streams on solar energetic particles. We also noted that there was a small eruption on 2022 February 16 around 15:00 UT observed by SOHO/LASCO on the west limb as seen from Earth. We have not ruled out that other solar events could be influencing the time profile at the locations of STEREO-A, Earth, and Solar Orbiter. To fully determine the source of these SEP events, a more detailed study of the remote-sensing observations of the Sun around the time of the main solar event

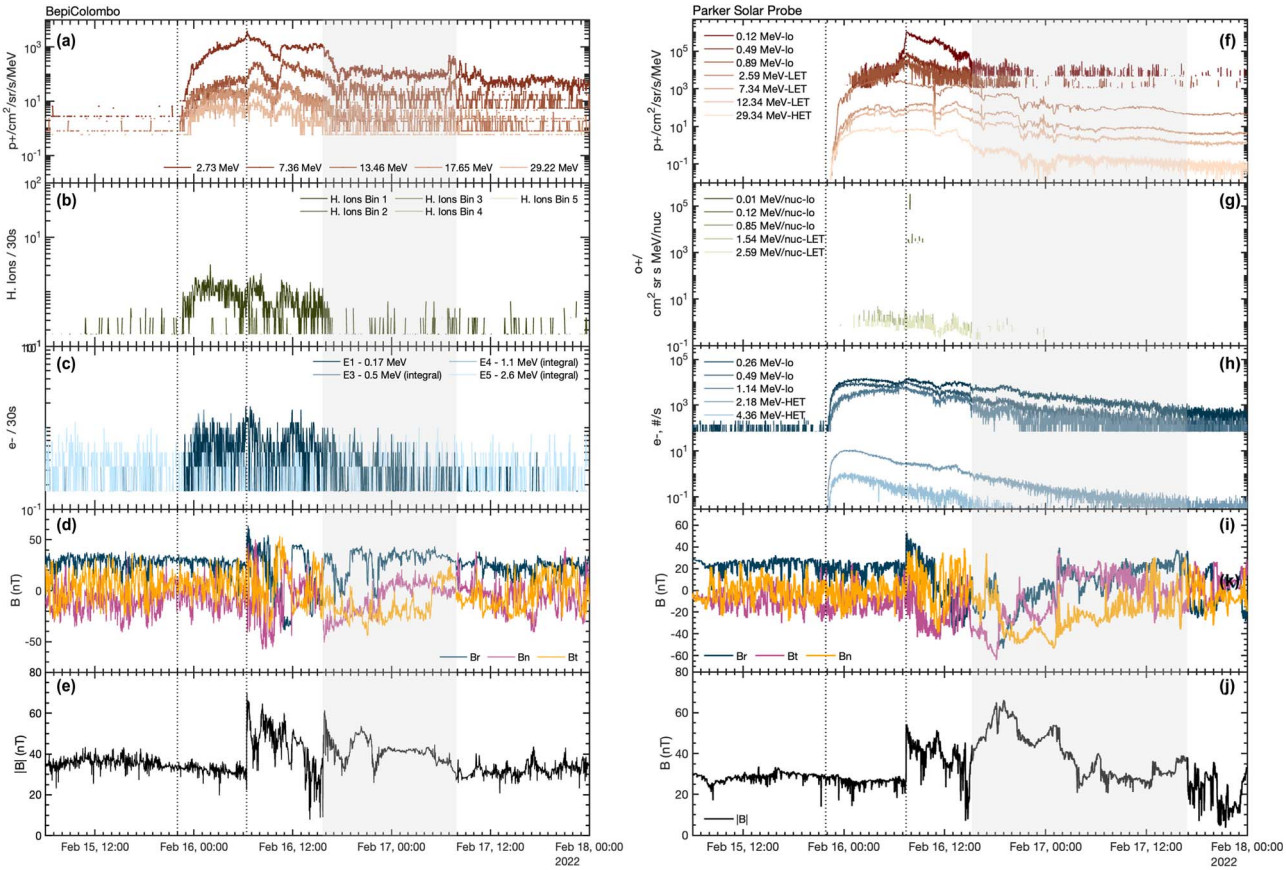

Figure 3. Overview of BepiColombo (left) and PSP (right) observations from 06:00 UT on 2022 February 15 to 00:00 UT on 2022 February 18. Panel (a): three-minute binned average proton flux from the BepiColombo/BERM instrument. Panels (b) and (c): three-minute binned average heavy ion and electron count rate, in units of #/30 s, from the BepiColombo/BERM instrument. Panels (d) and (c): In situ magnetic field in RTN coordinates and the total magnitude from the BepiColombo/MAG instrument. The highlighted gray region indicates the flux rope region that is likely associated with the CME ejecta. Panels (f), (g), and (h): three-minute binned average proton fluxes (away from the Sun) in units of #/(cm^2 sr s MeV), oxygen fluxes, and electron count rates from EPI-lo (Wedge 7), LET-B, and HET-B on board PSP. Panels (i) and (j): In situ magnetic field in RTN coordinates and its total magnitude from the PSP/FIELDS. The first dotted vertical line indicates the time when the radio bursts were observed by PSP at 21:50 UT on February 15, and the second dotted, vertical line represents the shock arrival at the individual spacecraft.

and in-depth analysis of the energetic particles are necessary. The latter would include detailed particle timing and anisotropies analysis and modeling of the transport of energetic particles, which are left for future studies.

4.2. Observations by BepiColombo and Parker Solar Probe

This section further investigates observations by BepiColombo and PSP during this event and compares their measurements.

Figure 3 (left) shows the particle time–intensity profile and the in situ magnetic field captured by the BERM and MPO-MAG instruments on BepiColombo at 0.35 au. About 10 minutes after the ejection at the Sun, at ∼22:00 UT on 2022 February 15 (indicated by the first dotted line), BERM observed an energetic electron event in all its channels (Figure 3(c)). Differential proton channels with energies above 1.44 MeV and at least up to 29 MeV were observed by BERM, accompanied by an increase in electrons (mainly ∼0.17 MeV electrons). We note that BepiColombo did not observe an obvious velocity dispersion from these first-arriving particles. For the first time since the launch of this mission, heavy ions were detected by the BERM instrument (Figure 3(b)), and the BERM instrument team is currently working on the calibration of these heavy ion channels.

BepiColombo observed the shock arrival around 06:30 UT on 2022 February 16 (second dotted line in Figure 3), approximately eight and a half hours after the first particles associated with the SEP event arrived at the spacecraft. The shock was clearly visible in the magnetic field data, which showed a sudden jump of ∼35 nT, as well as in the particle data, where a peak in the 2.73 MeV proton flux was observed at the same time (Figure 3(a)), suggesting a local acceleration mechanism related to the shock. Following the shock arrival was the sheath region that was present with a significant rotation in the three components of the magnetic field. We note that the changes in the magnetic field components also coincided with a dip in the proton fluxes (Figure 3(a)) and heavy ion count rates (Figure 3(b)). Following the sheath region was the magnetic ejecta as highlighted in light gray. The magnetic ejecta was characterized by a smooth rotation of the magnetic field, suggesting a flux rope-like structure, and lower energetic particle fluxes, as well as the presence of bidirectional suprathermal electron (not shown here; see Palmerio et al. (submitted) for more information). The trailing edge of the CME ejecta was accompanied by a small rise in the fluxes of particles that were piled up at the end of the flux rope, as well as the magnetic field returning to pre-CME values.

Figure 3 (right) shows the particle, magnetic field, and solar wind dynamics captured by PSP during this event. Given that

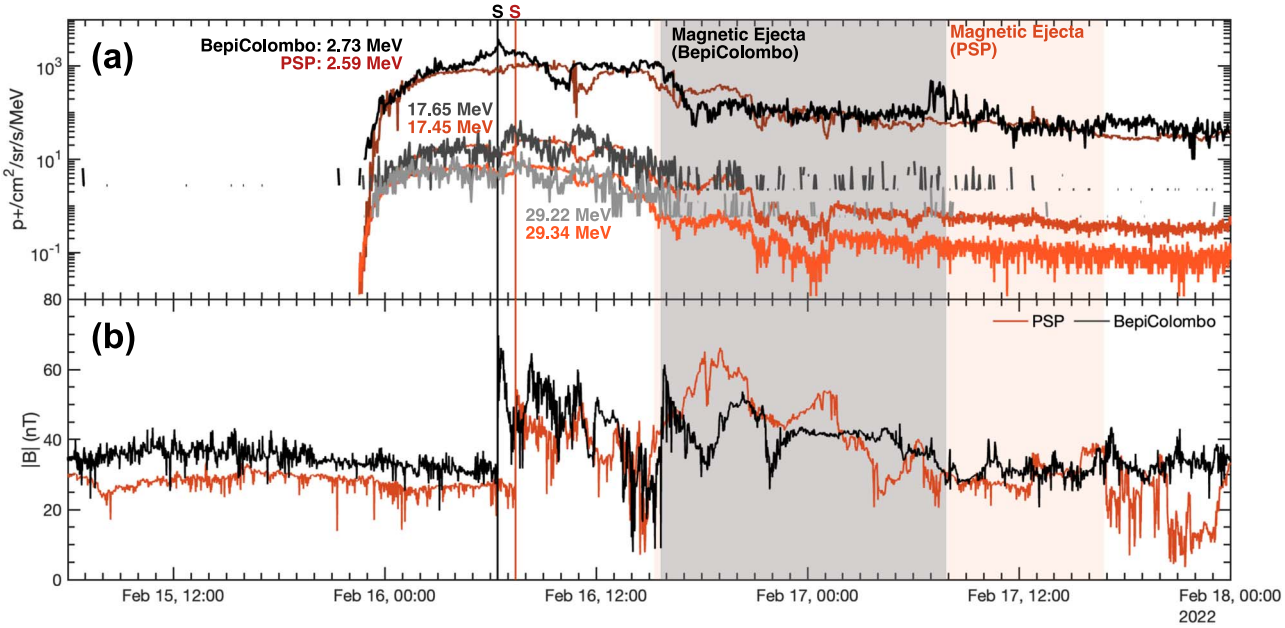

Figure 4. Comparison between PSP and BepiColombo measurements. (a) Comparison of one-minute resolution 2.59, 17.45, and 29.34 MeV proton fluxes from PSP (black/gray) with three-minute binned averaged 2.73, 17.65, and 29.22 MeV proton fluxes from BepiColombo (red/orange). (b) Comparison of the magnetic field magnitudes and their RTN components, respectively. Black and red solid lines represent PSP and BepiColombo data, respectively. The shaded gray and red regions indicate the magnetic ejecta observed on BepiColombo and PSP, respectively, while the black and red solid lines represent the shock arrival at BepiColombo and PSP.

the BERM instrument on board BepiColombo nominally points in an antisunward direction during the cruise phase (Pinto et al. 2021), we showed PSP measurements that were in the antisunward direction, including epi-Lo Wedge 7 (see Hill et al. 2017 for more details), LET-B, and HET-B.

PSP observed enhancements of 100 keV–60 MeV protons as well as heavy ions such as <1 MeV/nuc oxygen. These ions exhibited velocity dispersion where more energetic ions arrived first and were followed by lower-energy ions. A vast majority of the ions, including an increase in low-energy protons and heavy ions, arrived right after the shock arrival around 07:25 UT on February 16. While lower-energy protons (<1 MeV) experienced a sudden increase in flux at shock arrival, higher-energy protons experienced a more gradual increase near the shock and maintained the flux level for 2–3 hr after the shock arrival. The changes in the flux level inside the sheath region are likely associated with the rotation of the spacecraft (not shown). Within the flux rope (indicated by the shaded region), there are occasional particle dropouts as well as a suppression of the flux similar to the one observed by BepiColombo.

A few minutes after the radio bursts that were observed at 21:50 UT on February 15 (indicated by the first dotted line in Figure 3; see Appendix B for more details), PSP observed energetic electrons in the epi-lo/CHAN E data (Figure 3(h)), which is consistent with the almost-simultaneous appearance of the Langmuir waves (Figure A2). However, we note that most of the CHAN E data for >500 keV are likely overwhelmed by ions, which explains the similarity of the time–intensity profile between energetic electrons and energetic protons in Figures 3(h) and (f) (Mitchell et al. 2021). The >2 MeV electrons observed by the HET instrument followed a different trend than the CHAN E particles and were gradually decreasing after their initial arrival.

Figure 4 illustrates a direct comparison of the proton and magnetic field measurements from PSP and BepiColombo, which were almost colocated (with a radial separation of only 0.03 au). Because BERM on BepiColombo was pointing antisunward during this period, we compared the antisunward particle measurements from PSP with the BERM data from BepiColombo. This is the first time that a direct data comparison between PSP and BepiColombo has been performed, and this constitutes a rare opportunity for cross-calibration between these instruments.

The overall time variation of proton flux is illustrated in Figure 4(a), where black and red lines represent measurements from BepiColombo and PSP, respectively. Three different proton channels (2.6–30 MeV protons) demonstrate remarkable agreements with comparable fluxes observed between BepiColombo and PSP. A closer look at Figure 4(a) reveals some discrepancies; for instance, BepiColombo observed an energetic storm particle (ESP) event at 2.73 MeV, which was characterized by enhancements in flux observed at the shock arrival, while PSP did not observe the same ESP event at 2.59 MeV. The ESP events observed by PSP were limited to lower-energy particles (<1 MeV; Figure 3(f)). Giacalone et al. (2023) provide a detailed investigation of the ESP events observed by PSP during this event. It is important to note that the energy widths of these three proton channels are not the same for both spacecraft, and this difference is to be taken into account for cross-calibration in Appendix D. Notably, we observed the presence of an interesting three-slope spectrum with a plateau between 8 and 12 MeV near the shock (not shown here). A more detailed analysis of the evolution of the energy spectrum is ongoing to characterize and understand this interesting feature.

BepiColombo encountered the shock approximately an hour earlier than PSP, which is expected because BepiColombo was

closer to the Sun during this event. There is generally good agreement in the magnetic field between both spacecraft, in particular before and near the shock region (Figure 4(b)). Palmerio et al. (2023) provide a more detailed analysis of the mesoscale structure variation of the magnetic fields between the two spacecraft.

Seizing this unique opportunity, we performed the first cross-calibration between the BERM instrument on BepiColombo and the LET/HET instruments on PSP. We used ∼30 MeV protons that exhibited isotropic distribution for this analysis. Considerations like the energy width differences between the instruments and flux tube expansion (e.g., Levine et al. 1977) are taken into account for the cross-calibration analysis. Based on our analysis in Appendix D, we determined that the BERM flux measurements are generally ∼35% lower than the HET measurements, suggesting that an intercalibration factor of ∼1.35 is to be used to adjust BERM measurements to HET/LET measurements (see Appendix D for more details).

4.3. High-energy SEPs at Mars

During the SEP event, MSL/RAD observed the largest ground-level enhancement (GLE) at the surface of Mars, even larger than the 2017 September event (Zeitlin et al. 2018). Historically, a GLE event refers to enhancement detected by ground-based neutron monitors on Earth. In this study, we use the term "MGLE" to distinguish the ground-level enhancement event on Mars. Here, MGLE is defined as a large increase in the radiation dose measured by MSL/RAD in the Gale crater on the surface of Mars.

As illustrated in Figures 1 and A3 in the Appendix, the CME event was beyond the west limb from Mars' vantage point, and thus the CME structure did not impact Mars. Figure 5(c) shows that MSL/RAD began to detect a rapid rise above the galactic cosmic ray (GCR)-induced background levels in the surface radiation at 22:41 UT on 2022 February 15. At the peak of this event, the surface dose rates as measured by the MSL/RAD tissue-equivalent plastic scintillator increased by a factor of 3.5. This is significantly higher than the relative increase in dose rate in MSL/RAD measured during the 2017 September event, which peaked at an increase factor of around 2.2 (Zeitlin et al. 2018). The increase in the less-shielded MSL/RAD silicon detector, used for dose rate measurements, was similarly higher, with an increase in dose rate of a factor of ∼4.75, compared to an increase of a factor of ∼3 during the 2017 event (Zeitlin et al. 2018). The increase in the radiation dose rates is mainly caused by SEP protons with incident energies of >∼150 MeV penetrating through the Martian atmosphere down toward the surface (Guo et al. 2019).

Figure 5(a) shows the detection of such high-energy protons in orbit around Mars by MAVEN/SEP. In particular, the penetrating proton counts were measured in the MAVEN/SEP energy bins that are sensitive to protons with incident energies of 15–100 MeV (light blue) and 80–220 MeV (dark blue; see Section 4 in Lee et al. 2018 for further details). Meanwhile, the ASPERA-3 IMA instrument on board the MEX spacecraft measured penetrating background counts related to >1 MeV SEP electrons and >20 MeV protons (Ramstad et al. 2018) during the SEP activity, as shown in Figure 5(b). The onset times and sharp rise to the peak values of the MAVEN/SEP 80–220 MeV proton counts and the MEX/IMA penetrating particle counts are consistent with the MSL/RAD dose rate observations. We should note here that, to compare fluxes from the Martian orbit with fluxes from its surface, we need to account for the >150 MeV energy loss that protons encounter propagating through the Martian atmosphere to the surface. We should also note the large similarities between the fluxes obtained by PSP and BepiColombo and those measurements made by spacecraft in orbit at Mars, a sign of the good magnetic connectivity between these missions despite their "physical" angular distance.

Figure 5(c) shows that the MGLE event lasted nearly a day, with the peak surface radiation occurring at around 02:50 UT on 2022 February 16. Meanwhile, MAVEN/SEP observed the peak counts at around 06:27 UT on 2022 February 16 for the 80–220 MeV protons (dark blue line, Figure 5(a)), several hours after the peak in the surface dose rates. Figure 5(a) (light blue line) shows that, during this time, the 15–100 MeV proton counts reached their initial peak value, suggesting that the contributions in the peak of the 80–220 MeV proton counts at 06:27 UT are largely coming from protons at the lower-energy range (i.e., 80 MeV to less than 150 MeV). Members from both the MAVEN/SEP and MSL/RAD science teams are currently working on a more detailed analysis of the in situ measurements of the SEP protons at Mars to expand the understanding of the particle dynamics of this particular event as seen at Mars (Lee et al. 2023).

Figures 5(d) and (e) show that the 20 keV to 6 MeV SEP protons and 20–200 keV electrons were also observed during this event. A velocity dispersion pattern can be seen starting from the upper portion of the proton energy spectrogram (above a distinct <1 MeV proton population) on early February 16, where the highest-energy protons (∼6 MeV) arrived ahead of the lower-energy protons (∼20 keV), which arrived on February 18. This is consistent with the even earlier arrival of the 15–100 and 80–220 MeV proton counts shown in Figure 5(a), and it is also consistent with the west-limb orientation of the CME from Mars' vantage point. We note that a velocity dispersion pattern is also evident at the beginning of the SEP electron measurements by MAVEN/SEP, but this is not easily seen in Figure 5(d), given the large time range shown.

As shown in Figure 5(d), a dispersionless population of 20 keV to ∼1 MeV proton fluxes, distinct from the dispersive proton population described above, was also observed by MAVEN. This distinct population lasted for less than one day, between February 16 and 17. We note that several CMEs that erupted several days before February 16 were merged en route to 1.5 AU and likely impacted Mars around 06:00 UT on February 16 (see Figure A3(b) in Appendix C). It is likely that this distinct population of 20 keV to ∼1 MeV observed by MAVEN is associated with this merged CME, although we have not ruled out other possible sources for these SEP populations. For instance, an M-class solar flare was observed on the west limb of the Sun as seen from Earth around 18:00 UT on 2022 February 15. More in-depth modeling and analysis are necessary to understand the source of the energetic particles at Mars.

5. Discussion and Summary

This study presents multi-spacecraft observations of the third reported widespread solar energetic particle event in Solar Cycle 25. The eruption associated with this event was

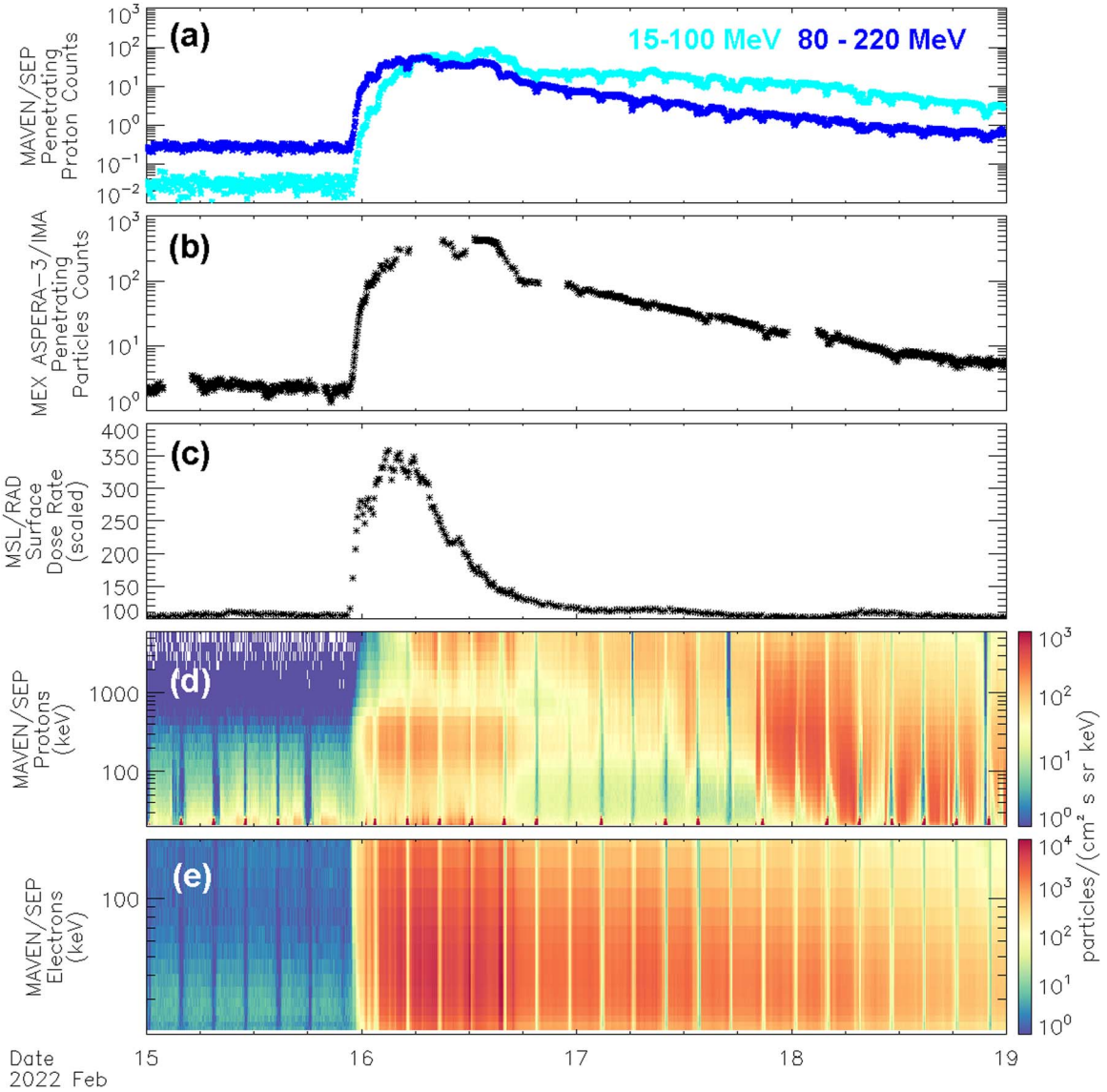

Figure 5. Particle dynamics on Mars. (a) Penetrating proton count rates from the SEP detector on board the MAVEN orbiter for 15–100 MeV protons (light blue) and 80–220 MeV protons (dark blue). (b) Penetrating particle count rates from the Mars Express ASPERA-3 IMA instrument. (c) Relative increase of Martian surface radiation dose rate scaled to the pre-event levels. Differential energy fluxes (colors) from MAVEN/SEP for (d) 20 keV to 6 MeV protons and (e) 20 to 200 keV electrons. The periodic drop in counts or fluxes seen in the MAVEN/SEP observations ((a), (d), and (e)) occur when MAVEN enters periapsis during its elliptical orbit around Mars.

previously reported as the most distant filament seen in EUV wavelengths (Mierla et al. 2022). Here, we present several notable SEP observations associated with this event.

First, SEPs were observed by multiple spacecraft across a longitudinal separation in magnetic footpoint between the eruption center and the spacecraft as high as ∼165°, which qualifies this as a widespread SEP event. The magnetic footpoints of BepiColombo, PSP, and Mars were closer to the eruption center during this event, and as expected, these spacecraft observed higher energetic proton fluxes compared to those measured by Solar Orbiter, STEREO-A, and near-Earth spacecraft such as Wind. The solar wind parameters and WSA–ENLIL simulation also indicate the arrival of stream interaction region (SIR) at Solar Orbiter, STEREO-A, and Earth during the SEP event, making it challenging to identify the source of these energetic particles. More detailed studies are underway to untangle the SIR-related and CME-related SEP events and to understand the underlying propagation and acceleration mechanism of energetic particles (Lee et al. 2023; Wei et al. 2023).

Second, BepiColombo and PSP were at ∼0.35–0.38 au with a radial separation of ∼0.03 au and a longitudinal separation of 3°–4° during this event. In fact, this is the first time that BepiColombo encountered heavy ion particles during the cruise phase, and a calibration of these channels is currently ongoing. A 3D CME reconstruction analysis suggests that PSP and BepiColombo likely encountered the CME southern flank, rather than the CME nose (see also Palmerio et al. 2023). Both spacecraft observed energetic protons and electrons soon after the radio burst observation at PSP and later measured a peak enhancement of energetic protons at the shock arrival, suggesting a locally shock-accelerated proton population. A detailed analysis of the ESP event, including the source of the accelerated particles, is available in Giacalone et al. (2023; see also Fraschetti & Goldberg 2023). In addition, we also noted an interesting three-slope energy spectrum near the shock, and a

more involved investigation is ongoing to characterize the evolution of the energy spectrum during this event.

The proximity of the two spacecraft also presents a precious opportunity for direct comparison and even cross-calibration. It is very important and useful to consolidate detections from both instruments, in particular for BepiColombo. Such an in-flight calibration of the instruments allows the instrument to be fully operational right after its orbit insertion at Mercury. A direct comparison between energetic particle (∼2–30 MeV) measurements from both spacecraft shows good agreement, which is not surprising given their proximity to each other, as shown in other studies like von Rosenvinge et al. (2009). We further performed cross-calibration and determined that the BERM flux measurements are generally ∼35% lower than the HET measurements after taking factors such as the difference in energy width and flux tube expansion into consideration. This suggests that an intercalibration factor of ∼1.35 for the channels used in this study is needed to adjust BERM measurements to HET/LET data. We note that this is a small correction factor, and it corroborates the good agreement between these instruments. Regarding the magnetic field, measurements from both spacecraft are generally in good agreement except in the magnetic ejecta region. For instance, PSP experienced a longer duration of magnetic ejecta, compared to BepiColombo. Interested readers are directed to our companion study, Palmerio et al. (2023), to learn more about the mesoscale structure of CMEs using BepiColombo and PSP.

Third, the Curiosity rover on the surface of Mars measured the largest ground-level enhancement since its operation during the same period. Such MGLE events are likely caused by >150 MeV protons, as discussed in Guo et al. (2019), and MAVEN indeed measured 80–200 MeV protons several hours after the MGLE event. Lower-energy protons and electrons were also observed by MAVEN when the MGLE event occurred. The detection of these lower-energy protons and electrons on Mars has important implications for space-weather effects on the Martian atmosphere. Given that only >150 MeV penetrating protons can cross the entirety of the Martian atmospheric column and produce an MGLE event (Guo et al. 2019), SEPs with lower energies deposit their energies in the Martian atmosphere, and the corresponding ion–neutral collisions produce absorption of radio frequencies crossing the ionosphere, which has strong implications for Mars' exploration, communications, and data relay from the surface (Sanchez-Cano et al. 2019). Although not shown, this event produced clear signs of signal degradation and even total attenuation on the two high-frequency radars currently in operation at Mars, namely the MARSIS radar on board MEX and the SHARAD radar on board the Mars Reconnaissance Orbiter. Given the importance of these space-weather-related effects produced by this SEP event, a separate study is ongoing, focusing on the response of the Martian system.

In summary, the 2022 February 15–16 widespread SEP event constitutes one of the most intense SEP events in the current solar cycle. Its fortuitous spacecraft configuration presents a unique opportunity to understand how energetic particles propagate, and possibly accelerate, in interplanetary space across a wide longitudinal range. This study presents an overview of the well-spread SEP event in the inner Solar System, reporting interesting features associated with this event, and provides the first BepiColombo-PSP particle detector intercalibration. In addition, it serves as an introduction to many ongoing studies that are being performed within the community, to collaboratively enhance our understanding of this SEP event.

Acknowledgments

This work is a product of a community effort to investigate the 2022 February 15–16 event under the coordination of an active working group and a best-effort basis collaboration between scientists from the missions involved in this work. It has benefited tremendously from many helpful discussions and from the collaborative spirit within its members.

L.Y.K. acknowledges support through IS⊙IS funding. B.S.-C. acknowledges support through STFC Ernest Rutherford Fellowship ST/V004115/1 and grant ST/Y000439/1. C.O.L. acknowledges support from the MAVEN project funded through the NASA Mars Exploration Program, the NASA LWS grants 80NSSC21K1325 and 80NSSC21K0119, and the NASA MDAP grant 80NSSC19K1224. L.R.-G. acknowledges the financial support by the Spanish Ministerio de Ciencia, Innovación y Universidades FEDER/MCIU/AEI Project PID2019-104863RB-I00/AEI/10.13039/501100011033 and by the European Union's Horizon 2020 research and innovation program under grant agreement No. 101004159 (SERPENTINE). A.K. acknowledges financial support from NASA NNN06AA01C (SO-SIS Phase-E, PSP EPI-Lo) contract. E.P. acknowledges support from NASA's PSP-GI (No. 80NSSC22K0349), O2R (No. 80NSSC20K0285), LWS (No. 80NSSC19K0067), and LWS-SC (No. 80NSSC22K0893) programs. F.C. acknowledges the financial support by an appointment to the NASA Postdoctoral Program at the NASA Goddard Space Flight Center, administered by ORAU through a contract with NASA, and the support of the Solar Orbiter mission. N.D., I.C.J., and A.F. are grateful for support by the Academy of Finland (SHOCKSEE, grant No. 346902). T.N.-C. acknowledges support through the Solar Orbiter mission (NASA). B.E. and the MSL/RAD data analysis are supported by NASA (SMD/Heliophysics and HEOMD/AES) under JPL subcontract #1273039 to Southwest Research Institute. V.K. received support from the STEREO/Waves and Wind/Waves projects.

We gratefully thank everyone who helped make the IS⊙IS instrument suite and PSP mission possible. The IS⊙IS data and visualization tools are available at https://spacephysics.princeton.edu/missions-instruments/isois. PSP was designed, built, and is operated by the Johns Hopkins Applied Physics Laboratory as part of NASA's Living with a Star (LWS) program (contract NNN06AA01C). We are also thankful to the BepiColombo MAG and BERM teams who provided the data and assisted the data interpretation. Solar Orbiter is a space mission of international collaboration between ESA and NASA, operated by ESA. SOHO is a project of international cooperation between ESA and NASA. LASCO was constructed by a consortium of institutions: the Naval Research Laboratory (Washington, DC, USA), the Max-Planck-Institut fur Aeronomie (Katlenburg-Lindau, Germany), the Laboratoire d'Astronomie Spatiale (Marseille, France), and the University of Birmingham (Birmingham, UK).

ENLIL simulation results have been provided by the CCMC at NASA Goddard Space Flight Center (GSFC) through their public Runs-on-Request system (http://ccmc.gsfc.nasa.gov; run ID Christina_Lee_101722_SH_1). The WSA model was

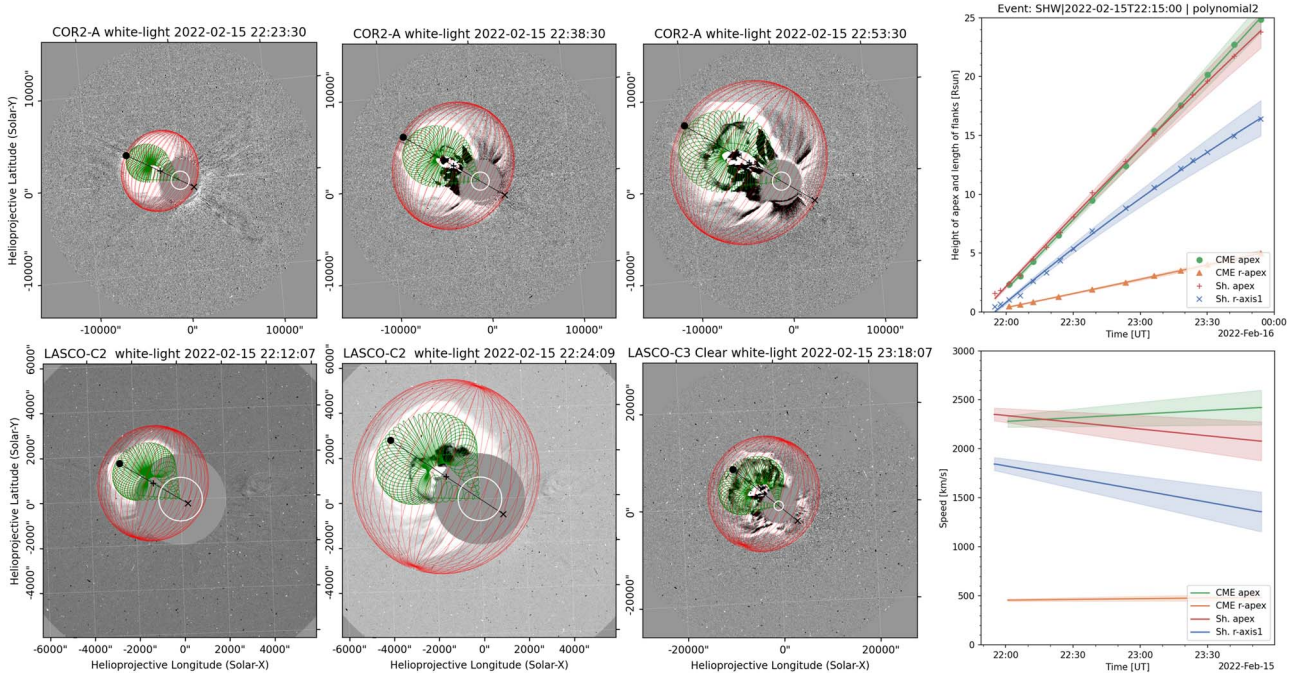

Figure A1. CME and shock wave 3D reconstruction results. Left: STEREO A/COR2 (top) and SOHO/LASCO observations (bottom) at different instants of time. The green (red) mesh corresponding to the 3D reconstruction of the CME (shock) is overlaid to running-difference images. Right: Height (top) and speed (bottom) of the CME and shock apex. Details given in main text.

developed by N. Arge, currently at NASA/GSFC, and the ENLIL Model was developed by D. Odstrcil, currently at George Mason University. Finally, L.Y.K. would like to thank the Princeton Space Physics research group for their useful suggestions and feedback that helped improve the quality of this article.

Appendix A
CME and Shock Wave

We reconstructed the CME using base-difference coronagraphic images from white-light coronagraphs on board STEREO/SECCHI-A (COR1 and COR2) as well as SOHO/LASCO (C2 and C3). The shock reconstruction was based on running-difference images of the same coronagraphs and including the Extreme UltraViolet Imager (EUVI) part of STEREO/SECCHI-A at 195 Å as well as SDO/AIA at 193 Å. To perform the 3D reconstruction, we used PyThea, a software package written in Python that can be used to reconstruct the 3D structure of CMEs and shock waves (Kouloumvakos et al. 2022b). Throughout the fitting process, we adjusted the free parameters of the Graduated Cylindrical Shell (GCS; Thernisien et al. 2006, 2009) and ellipsoid model to fit the CME and shock observations from the two viewpoints. The deviations in the parameters of the GCS analysis are given in Table 2 of Thernisien et al. (2009). Since the separation angle of the observers from which we utilized imaging data (i.e., STEREO-A, SOHO, and SDO) was small and the orientation of this event was close to the image plane of STEREO-A, there is some uncertainty (e.g., Verbeke et al. 2022) on the true width of the CME and the shock wave at the flanks in the east–west direction, which is difficult to model. However, as seen in Figure A1, the extension of the shock was remarkably broad, reaching coronal regions with an angular separation from the source region of more than 120°.

We started the CME reconstruction at ∼22:12 UT, when the flux rope was best observed in white light by STEREO/COR1-A, and we continued until ∼23:54 UT, when the CME reached LASCO/C3 field of view. For the shock wave, we started the fitting process earlier, at ∼21:55 UT, when the shock wave was low in the corona and it was observed as an EUV wave in STEREO/EUVI-A and SDO/AIA images. EUV waves are considered to be fast-mode waves or shocks that are initially CME-driven in the low corona (e.g., Cheng et al. 2012; Patsourakos & Vourlidas 2012; Long et al. 2017). We continued our shock fittings using the coronagraphic images until ∼00:18 UT on February 16, when the shock was at ∼26 $R_\odot$ in the field of view of LASCO/C3. After that time, the shock front became faint and difficult to trace.

Figure A1 shows the 3D reconstructed CME (green mesh) and shock (red mesh), where the wire frame is overlaid on top of STEREO/SECCHI/COR2-A (top panels) and SOHO/LASCO/C2 and C3 images (bottom panels) for three different times. The 3D reconstruction shows that the CME parameters do not display deviations, being the longitude and latitude of the CME apex −134° and 33°, respectively. The tilt angle stays at fixed values of −50°. The width of the CME is estimated based on Dumbović et al. (2019), where the semi-angular extent in the equatorial plane is expressed by $R_{\rm maj} - (R_{\rm maj} - R_{\rm min}) \times |{\rm tilt}|/90$. The total angular extent of the CME is estimated to be 58°. The value of $R_{\rm maj}$ (face-on CME half-width) is calculated by adding $R_{\rm min}$(edge-on CME half-width) to the half-angle, and $R_{\rm min}$ was calculated as the arcsin (aspect ratio). The CME width deviation was derived from the mean half-angle error, estimated by Thernisien et al. (2009) as +13°/−7°.

The shock apex is close to the CME nose, whereas the shock flanks are more distant from the CME legs. From the 3D reconstruction, we find that the height of the shock apex is slightly larger than the CME height at the nose. Additionally,

the shock wave in the coronagraphic images seems to engulf the whole Sun, and distant streamers seem to be pushed by the shock. We find that the propagation direction of the shock is at an average longitude of ∼124° in the Stonyhurst coordinate system. The CME-driven shock speed is estimated to be ∼2315 km s^{-1} (±185 km s^{-1}, which is ±8% of the determined value; Kwon et al. 2014) at a heliocentric height of 25 $R_{\odot}$.

The height of the CME and shock apex from the reconstruction is seen in Figure A1. Additionally, it shows the length of one of the semi-axes of the ellipsoid and the radius of the CME flux rope at the apex. We fit a second-order polynomial to the height(length)–time profiles to calculate the CME and shock wave kinematics. The bottom right panel of Figure A1 illustrates the CME and shock speed profile. The CME speed at the leading edge estimated from the linear fit to the height–time measurements is 2376 km s^{-1}(±166 km s^{-1}, which is ±7% of the estimated speed; Kwon et al. 2014).

Thus, at the latest time of the 3D reconstruction at 23:54 UT, corresponding to a CME height of 25 $R_{\odot}$, the not-so-wide CME (∼58°) is propagating in the direction E134N33 with a high speed (∼2376 km s^{-1}).

Appendix B
Interplanetary Radio Burst Measurements and Connectivity Analysis

Solar radio bursts serve as a robust diagnostic instrument to decipher energy release mechanisms and particle acceleration processes during solar flares (Wild 1950; Ginzburg & Zhelezniakov 1958). Electron beams trigger Type II bursts as they accelerate at shock fronts driven by rapid CME movements. Conversely, Type III bursts arise from impulsively accelerated electrons, associated with solar flares and coronal jets (Reiner et al. 1998; Gopalswamy et al. 2000; Reiner et al. 2001). The pronounced SEP event from 2022 February 15 to 16 correlated with a complex Type III burst initiated around 21:50 UT, as captured by PSP, Solar Orbiter, STEREO-A, and Wind (Bougeret et al. 1995, 2008; Bale et al. 2016; Maksimovic et al. 2020). PSP also recorded local Langmuir waves around 22:15 UT on February 15. This suggests that beamed energetic electrons generating the type III radio bursts traversed the vicinity of the probe (Larosa et al. 2021; Jebaraj et al. 2023). The waves were observed for a prolonged period from 22:15 until 23:45 UT, which also implies a prolonged connection between the probe and the energetic electron source.

The Type III burst was succeeded by a Type II burst, observed by PSP, STEREO-A, and Wind (refer to Figure A2(a)-Asd). The heightened noise level at Solar Orbiter led to the nondetection of the Type II burst (Maksimovic et al. 2021). To pinpoint the Type III burst's location in interplanetary space (illustrated in Figure A2(e)), we employed two distinct methodologies. Initially, direction-finding data recorded by STEREO-A and Wind were utilized (Krupar et al. 2014). Subsequently, we adopted a novel localization approach from Krupar et al. 2024, premised on the assumption of a circular Gaussian distribution of radio flux within the inner heliosphere. Both techniques concurred, suggesting the direction of Type III burst propagation aligned closely to the trajectory of the PSP. Regrettably, neither method was apt for analyzing Type II bursts, due to their detection only at elevated

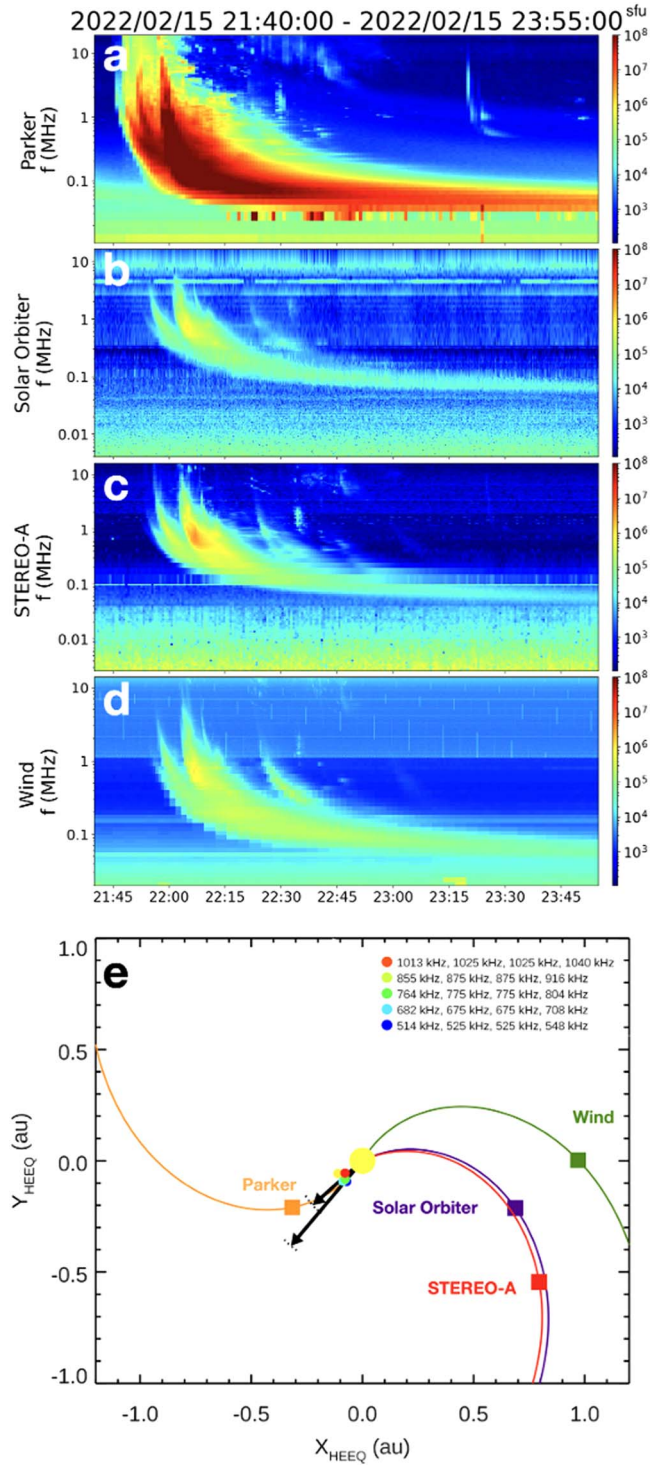

Figure A2. Radio spectra of the Type III burst recorded on 2022 February 15 by four spacecraft: (a) Parker Solar Probe, (b) Solar Orbiter, (c) STEREO-A, and (d) Wind. (e) Granular spatial distribution of spacecraft and radio sources in the HEEQ coordinate system. The colored rectangles highlight the spacecraft positions, while their paths are delineated by Parker spirals, extrapolated from an assumed solar wind speed of 400 km s^{-1}. The event's triangulated radio source positions are indicated by unique colored circles. Two contrasting black arrows denote the average azimuths ascertained by two strategies: the elongated arrow embodies intensity fitting, while the abbreviated arrow symbolizes radio triangulation. To elucidate each method's precision, dotted black perimeters encircle these arrows' termini, acting as visual metaphors for the angular error bars.

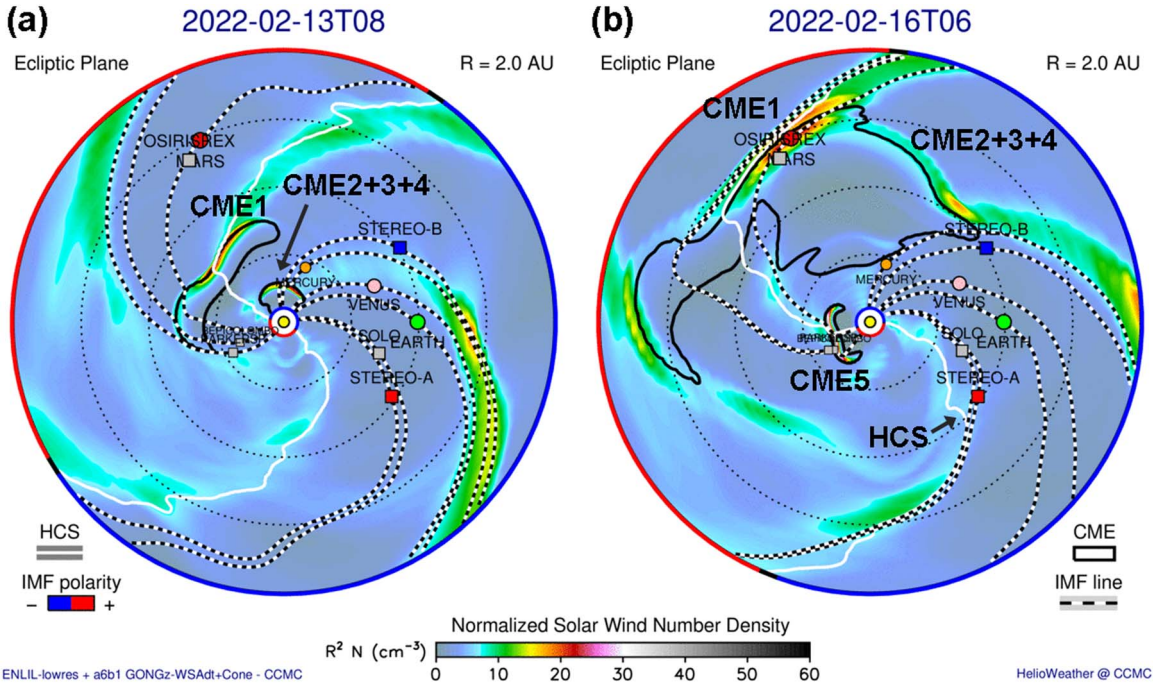

Figure A3. WSA–ENLIL simulation snapshots showing the eruption and evolution of several CMEs (CME1 and the merged CME2+3+4 structure) that erupted on 2022 February 11, 12, and 14, prior to the CME eruption on 2022 February 15 (CME5). The colors shown are the scaled solar wind densities in the ecliptic plane. The black and white dashed lines represent the IMF lines, and the black contours track the ICMEs. The white lines correspond to the heliospheric current sheet (HCS), which separates the regions with opposite magnetic polarity, shown in blue (negative) or red (positive) on the outer edge of the simulation region.

frequencies. Though one might anticipate the direction to be pointing toward the PSP, this is not consistently observed, as elucidated recently by Krupar et al. (2016).

Appendix C
Discussion of WSA–ENLIL Modeling Results

To obtain a global context of the interplanetary conditions experienced at the locations of SolO, Bepi, PSP, Mars, STEREO-A, and Earth during the SEP event, simulations of the CME propagation through the ambient solar wind were made at the NASA Community Coordinated Modeling Center's Runs-on-Request page (https://ccmc.gsfc.nasa.gov/tools/runs-on-request/). In particular, the Wang–Sheeley–Arge solar corona model and the 3D MHD ENLIL solar wind model (hereafter WSA–ENLIL; Arge & Pizzo 2000; Odstrcil 2003, 2023) were used in tandem to model the propagation of several ICMEs, including the main ICME event of this study. Figure A3 shows two simulation snapshots of the ecliptic solar wind density (scaled by r2) and the positions of the planets and spacecraft that are located within the radial distance of 2 AU. The black contours in Figures A3(a) and (b) show the parameterized clouds for four ICMEs that erupted on the 11th (CME1), 12th (CME2 and CME3), and 14th (CME4) prior to our main ICME event that erupted on the 15th (CME5), which is shown in Figure A3(b) only.

The snapshots in Figure A3 were selected to illustrate the disturbed conditions caused by the impacts of CME1 and the merged CME2+3+4 structures at Mars when the main ICME event that was described in Section 3.1 erupted. The dashed black and white lines that thread through Mars in both panels suggest that Mars maintained its connection to the CME1 shock front while being magnetically connected to CME5 during the early phase of this event. Meanwhile, Figure A3(b) was also selected to illustrate the complexities associated with analyzing the SEP measurements at the STEREO-A, SolO, and Earth locations. The snapshot shows the presence of a dense solar wind stream together with the heliospheric current sheet structure when the eruption occurred on 2022 February 15 CME.

Further details regarding the modeling of the propagation of the ICMEs that impacted Mars during this event period, including the modeling of the transport of the associated SEPs, will be described in a future publication (e.g., Lee et al. 2023). Meanwhile, the WSA–ENLIL simulation results shown in Figure A3 may be found at the CCMC results output page (https://ccmc.gsfc.nasa.gov/results/viewrun.php?domain=SH&runnumber=Christina_Lee_101722_SH_1), which includes the details of the input CME values used when initiating the WSA–ENLIL simulation.

Appendix D
Intercalibration between BepiColombo/BERM and PSP/HET

There are several steps necessary to properly perform a cross-calibration between these instruments. First, we identified energy channels that exhibited isotropic particle distribution by comparing the ratio between sunward and antisunward measurements on LET and HET (see Figures A4 and A5). As shown in Figure A5, 29 MeV protons displayed an isotropic distribution, as compared to lower-energy channels such as 2.6 MeV. Therefore, we used the 29 MeV proton channel for the rest of the analysis, assuming that the flux observed by BepiColombo at ∼29 MeV also observed an isotropic flux at the same time.

Second, because the energy width of the BERM instrument (20.7–31.4 MeV) is wider than that of the HET instrument (27–32 MeV), we determined the average flux for HET over a wider range of energy (19–32 MeV) and used the average flux values for the rest of the analysis.

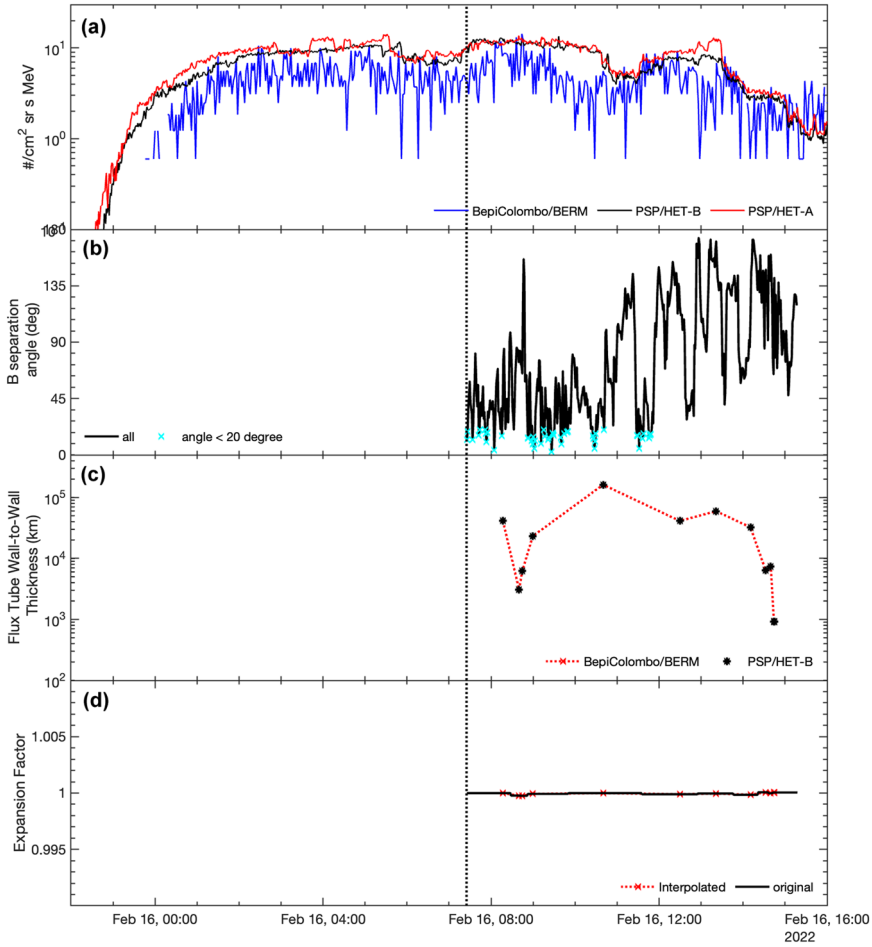

Figure A4. Intermediate results for the cross-calibration analysis between the BERM and HET instruments. (a) 29 MeV proton flux variation observed by HET-B (black) and HET-A (red) between 22:00 UT on February 15 and 06:00 UT on February 16. The blue line is the one hour, time-shifted proton flux from BERM such that the shock arrival on BERM coincided with that from PSP. (b) Separation angle of the magnetic field vectors (in RTN coordinate) between BepiColombo/BERM and PSP/HET instrument. The cyan cross indicates the region where the separation angle $< 20°$. (c) Flux tube wall-to-wall thickness (km) that was determined using the methodology described in Borovsky (2008). (d) Flux tube expansion factor computed from the ratio of flux tube wall-to-wall thickness experienced by BepiColombo and PSP. See text for more details.

Third, to ensure the instruments are measuring a similar population, we further assessed if the trend of energetic proton time–intensity profile is within reasonable agreement by time-shifting proton flux measurements from BERM by one hour, such that the shock arrival time at BepiColombo coincided with that at PSP. As shown in Figure A4(a), the general trend of time-shifted BERM proton fluxes matches well with the PSP proton measurements.

We then identified regions where the two spacecraft are experiencing a relatively similar magnetic structure, which is defined as a separation angle of the magnetic field vector between two spacecraft (i.e., the dot product of their magnetic field vector in RTN coordinate) is less than 20°. We only examined the separation angle after the shock arrival. The identified regions are indicated by cyan crosses in Figure A4(c). The proton flux measured by the sunward-pointing instrument (LET-A and HET-A from PSP) collected with this condition is plotted against proton flux measured by the antisunward-pointing instruments, LET-A and HET-B from PSP (black) as well as BERM from BepiColombo (red), in Figure A5.

For those particles, we further estimated the flux expansion factor (the ratio between the area of the flux tube at PSP and that at BepiColombo) from one spacecraft to the other. Assuming that particle flux remains invariant along a flux tube, as particles did not experience any scattering or loss during propagation, particle flux observed at different points of observations along a flux tube should decrease in intensity as the flux tube expands radially outward (e.g., Levine et al. 1977). In other words, $j{\cdot}A$ is approximately constant, where j is particle flux and A is the area of the flux tube. We followed the methodology described in Borovsky (2008) to identify the flux tube boundary and compute the flux tube wall-to-wall thickness, which is proportional to the radius of the flux tube. Because it requires solar wind speed in order to estimate the flux wall-to-wall thickness, we assume BepiColombo experienced the same solar wind speed as PSP. Figure A4(e) shows that the flux expansion ratio from BepiColombo to PSP was very close to 1, suggesting that flux variations from BepiColombo to PSP due to flux tube expansion should be negligible.

Finally, we computed the ratio of antisunward HET (HET-B) flux and BERM flux and fit a log-normal curve on the histogram of the flux ratio (Figure A5(b)). The result indicates that most of the measurements are within 1.35 with a full width at half maximum of 1.60, suggesting a good agreement

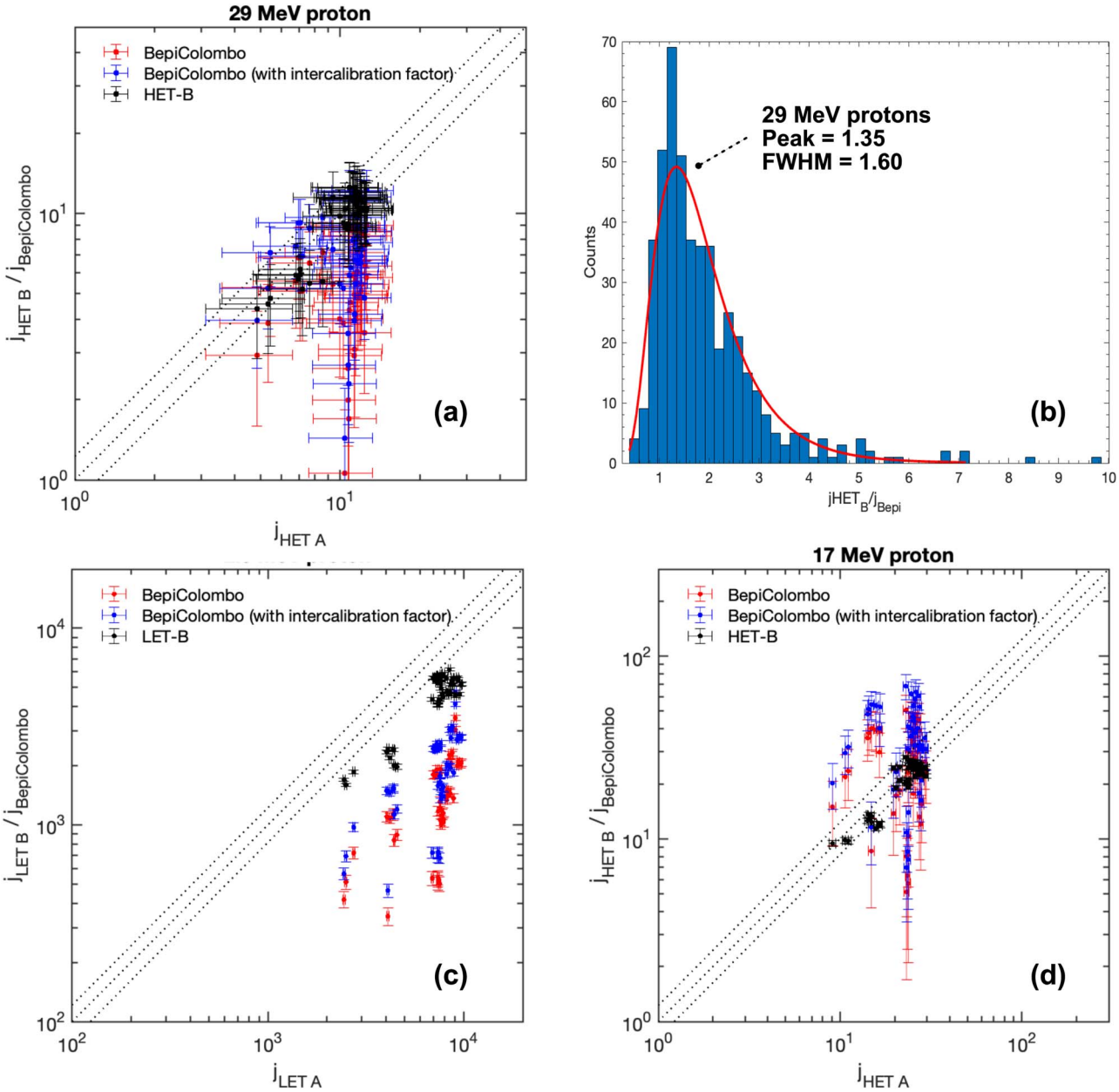

Figure A5. Panel (a): Plots of 29 MeV proton sunward data from PSP (HET-A) against antisunward data from PSP (HET-B; indicated by black dots) and BepiColombo (red and blue dots for those before and after including the intercalibration factor, respectively). Only data from when the magnetic field separation angle between PSP and BepiColombo is less than 20° are included in this plot. Dotted black lines indicate lines where the sunward data matches the antisunward data (center line) with ±20% uncertainty. Panel (b): Histogram of the flux ratio between HET-B and BepiColombo for 29 MeV proton channel with a log-normal fitted curve (red). Panels (c) and (d): plots similar to those in (a), but for 2.6 and 17 MeV, respectively.

between the BERM and HET instruments. Because the HET and LET instruments on PSP are generally well-calibrated with each other (Joyce et al. 2021), this also suggests that the BERM instrument likely matches well with the PSP/LET instrument, using an intercalibration factor of 1.35. We note that, in the presence of anisotropic flux distribution, BERM and LET/HET are likely to measure particles from different pitch angles and therefore display some flux discrepancies (as shown in Figures A5(a) and (b)). This is the first time that these two instruments have been cross-calibrated. Further analysis, and potentially more events in which both spacecraft are in a similar configuration, will be needed in order to fully intercalibrate the rest of the channels from these two instruments.

ORCID iDs

L. Y. Khoo https://orcid.org/0000-0003-0412-1064
B. Sánchez-Cano https://orcid.org/0000-0003-0277-3253
C. O. Lee https://orcid.org/0000-0002-1604-3326
L. Rodríguez-García https://orcid.org/0000-0003-2361-5510
A. Kouloumvakos https://orcid.org/0000-0001-6589-4509
E. Palmerio https://orcid.org/0000-0001-6590-3479
F. Carcaboso https://orcid.org/0000-0003-1758-6194
D. Lario https://orcid.org/0000-0002-3176-8704
N. Dresing https://orcid.org/0000-0003-3903-4649
C. M. S. Cohen https://orcid.org/0000-0002-0978-8127
D. J. McComas https://orcid.org/0000-0001-6160-1158

B. J. Lynch https://orcid.org/0000-0001-6886-855X
F. Fraschetti https://orcid.org/0000-0002-5456-4771
I. C. Jebaraj https://orcid.org/0000-0002-0606-7172
J. G. Mitchell https://orcid.org/0000-0003-4501-5452
T. Nieves-Chinchilla https://orcid.org/0000-0003-0565-4890
V. Krupar https://orcid.org/0000-0001-6185-3945
D. Pacheco https://orcid.org/0000-0002-6176-4077
J. Giacalone https://orcid.org/0000-0002-0850-4233
J. Benkhoff https://orcid.org/0000-0002-4307-9703
X. Bonnin https://orcid.org/0000-0003-4217-7333
E. R. Christian https://orcid.org/0000-0003-2134-3937
B. Ehresmann https://orcid.org/0000-0002-5956-5722
D. Fischer https://orcid.org/0000-0002-8435-7220
D. Heyner https://orcid.org/0000-0001-7894-8246
M. Holmström https://orcid.org/0000-0001-5494-5374
R. A. Leske https://orcid.org/0000-0002-0156-2414
M. Maksimovic https://orcid.org/0000-0001-6172-5062
J. Z. D. Mieth https://orcid.org/0000-0002-7539-0803
P. Oleynik https://orcid.org/0000-0003-0794-7742
M. Pinto https://orcid.org/0000-0002-5712-9396
I. Richter https://orcid.org/0000-0002-5324-4039
J. Rodríguez-Pacheco https://orcid.org/0000-0002-4240-1115
N. A. Schwadron https://orcid.org/0000-0002-3737-9283
D. Schmid https://orcid.org/0000-0001-7818-4338
D. Telloni https://orcid.org/0000-0002-6710-8142
A. Vecchio https://orcid.org/0000-0002-2002-1701
M. E. Wiedenbeck https://orcid.org/0000-0002-2825-3128

References

Arge, C. N., & Pizzo, V. J. 2000, JGR, 105, 10465
Bale, S. D., Goetz, K., Harvey, P. R., et al. 2016, SSRv, 204, 49
Barabash, S., Lundin, R., Andersson, H., et al. 2006, SSRv, 126, 113
Benkhoff, J., Murakami, G., Baumjohann, W., et al. 2021, SSRv, 217, 90
Borovsky, J. E. 2008, JGR, 113, A08110
Bougeret, J. L., Goetz, K., Kaiser, M. L., et al. 2008, SSRv, 136, 487
Bougeret, J. L., Kaiser, M. L., Kellogg, P. J., et al. 1995, SSR, 71, 231
Brueckner, G. E., Howard, R. A., Koomen, M. J., et al. 1995, SoPh, 162, 357
Cane, H. V. 1996, AIPC, 374, 124
Cane, H. V., Reames, D. V., & von Rosenvinge, T. T. 1988, JGR, 93, 9555
Cheng, X., Zhang, J., Olmedo, O., et al. 2012, ApJL, 745, L5
Chicarro, A., Martin, P., & Trautner, R. 2004, in Mars Express: The Scientific Payload, ed. A. Wilson & A. Chicarro (Noordwijk: ESA Publications Division), 3
Cohen, C. M. S., Christian, E. R., Cummings, A. C., et al. 2021, A&A, 656, A29
Cohen, C. M. S., Mason, G. M., & Mewaldt, R. A. 2017, ApJ, 843, 132
de Lucas, A., Schwenn, R., dal Lago, A., Marsch, E., & Clúa de Gonzalez, A. L. 2011, JASTP, 73, 1281
Domingo, V., Fleck, B., & Poland, A. I. 1995, SoPh, 162, 1
Dresing, N., Gómez-Herrero, R., Heber, B., et al. 2014, A&A, 567, A27
Dresing, N., Gómez-Herrero, R., Klassen, A., et al. 2012, SoPh, 281, 281
Dresing, N., Rodríguez-García, L., Jebaraj, I. C., et al. 2023, A&A, 674, A105
Dumbović, M., Guo, J., Temmer, M., et al. 2019, ApJ, 880, 18
Fox, N. J., Velli, M. C., Bale, S. D., et al. 2016, SSRv, 204, 7
Fraschetti, F., & Goldberg, G. 2023, in AGU Fall Meeting, SH31E–3022
Futaana, Y., Shimoyama, M., Wieser, M., et al. 2022, ApJ, 940, 178
Galvin, A. B., Kistler, L. M., Popecki, M. A., et al. 2008, SSRv, 136, 437
Giacalone, J., Cohen, C. M. S., McComas, D. J., et al. 2023, ApJ, 958, 144
Giacalone, J., & Jokipii, J. R. 2012, AIPC, 1436, 130
Gieseler, J., Dresing, N., Palmroos, C., et al. 2023, FrASS, 9, 1058810
Ginzburg, V. L., & Zhelezniakov, V. V. 1958, SvA, 2, 653
Gold, R. E., Krimigis, S. M., Hawkins, S. E., et al. 1998, SSRv, 86, 541
Gómez-Herrero, R., Dresing, N., Klassen, A., et al. 2015, ApJ, 799, 55
Gopalswamy, N., Lara, A., Lepping, R. P., et al. 2000, GeoRL, 27, 145
Grotzinger, J. P., Crisp, J., Vasavada, A. R., et al. 2012, SSRv, 170, 5
Guo, J., Wimmer-Schweingruber, R. F., Wang, Y., et al. 2019, ApJL, 883, L12
Hadid, L. Z., Génot, V., Aizawa, S., et al. 2021, FrASS, 8, 718024
Hassler, D. M., Zeitlin, C., Wimmer-Schweingruber, R. F., et al. 2012, SSRv, 170, 503
Heyner, D., Auster, H.-U., Fornaçon, K.-H., et al. 2021, SSRv, 217, 52
Horbury, T. S., O'Brien, H., Carrasco Blazquez, I., et al. 2020, A&A, 642, A9
Hill, M. E., Mitchell, D. G., Andrews, G. B., et al. 2017, JGRA, 122, 1513
Howard, R. A., Moses, J. D., Vourlidas, A., et al. 2008, SSRv, 136, 67
Jakosky, B. M., Lin, R. P., Grebowsky, J. M., et al. 2015, SSRv, 195, 3
Jebaraj, I. C., Krasnoselskikh, V., Pulupa, M., Magdalenic, J., & Bale, S. D. 2023, ApJL, 955, L20
Joyce, C. J., McComas, D. J., Schwadron, N. A., et al. 2021, A&A, 651, A2
Kaiser, M. L., Kucera, T. A., Davila, J. M., et al. 2008, SSRv, 136, 5
Kasper, J. C., Abiad, R., Austin, G., et al. 2016, SSRv, 204, 131
Kollhoff, A., Kouloumvakos, A., Lario, D., et al. 2021, A&A, 656, A20
Kouloumvakos, A., Kwon, R. Y., Rodríguez-García, L., et al. 2022a, A&A, 660, A84
Kouloumvakos, A., Nindos, A., Valtonen, E., et al. 2015, A&A, 580, A80
Kouloumvakos, A., Rodríguez-García, L., Gieseler, J., et al. 2022b, FrASS, 9, 974137
Krupar, V., Eastwood, J. P., Kruparova, O., et al. 2016, ApJL, 823, L5
Krupar, V., Maksimovic, M., Santolik, O., et al. 2014, SoPh, 289, 3121
Krupar, V., Kruparova, O., Szabo, A., et al. 2024, ApJ, 961, 88
Kwon, R.-Y., Zhang, J., & Olmedo, O. 2014, ApJ, 794, 148
Laitinen, T., Huttunen-Heikinmaa, K., Valtonen, E., & Dalla, S. 2015, ApJ, 806, 114
Lario, D., Kwon, R. Y., Richardson, I. G., et al. 2017, ApJ, 838, 51
Lario, D., Kwon, R. Y., Vourlidas, A., et al. 2016, ApJ, 819, 72
Lario, D., Raouafi, N. E., Kwon, R. Y., et al. 2014, ApJ, 797, 8
Larosa, A., Krasnoselskikh, V., Dudok de Wit, T., et al. 2021, A&A, 650, A3
Larson, D. E., Lillis, R. J., Lee, C. O., et al. 2015, SSRv, 195, 153
Lee, C. O., Dunn, P., Ehresmann, B. E., et al. 2023, in AGU Fall Meeting, P43H–3366
Lee, C. O., Jakosky, B. M., Luhmann, J. G., et al. 2018, GeoRL, 45, 8871
Lemen, J. R., Title, A. M., Akin, D. J., et al. 2012, SoPh, 275, 17
Lepping, R. P., Acuña, M. H., Burlaga, L. F., et al. 1995, SSRv, 71, 207
Levine, R. H., Altschuler, M. D., & Harvey, J. W. 1977, JGR, 82, 1061
Lin, R. P., Anderson, K. A., Ashford, S., et al. 1995, SSRv, 71, 125
Long, D. M., Bloomfield, D. S., Chen, P. F., et al. 2017, SoPh, 292, 7
Luhmann, J. G., Curtis, D. W., Schroeder, P., et al. 2008, SSRv, 136, 117
Maksimovic, M., Bale, S. D., Chust, T., et al. 2020, A&A, 642, A12
Maksimovic, M., Souček, J., Chust, T., et al. 2021, A&A, 656, A41
Mangano, V., Dósa, M., Fränz, M., et al. 2021, SSRv, 217, 23
McComas, D. J., Alexander, N., Angold, N., et al. 2016, SSRv, 204, 187
Mierla, M., Zhukov, A. N., Berghmans, D., et al. 2022, A&A, 662, L5
Mitchell, J. G., De Nolfo, G. A., Hill, et al. 2021, ApJ, 919, 119
Montagnon, E., Budnik, F., Casale, M., et al. 2021, SSRv, 217, 32
Müller, D., Nicula, B., Felix, S., et al. 2017, A&A, 606, A10
Müller St., D., Cyr, O. C., Zouganelis, I., et al. 2020, A&A, 642, A1
Müller-Mellin, R., Kunow, H., Fleißner, V., et al. 1995, SoPh, 162, 483
Odstrcil, D. 2003, AdSpR, 32, 497
Odstrcil, D. 2023, FrASS, 10, 1226992
Ogilvie, K. W., Chornay, D. J., Fritzenreiter, R. J., et al. 1995, SSRv, 71, 55
Ogilvie, K. W., & Desch, M. D. 1997, AdSpR, 20, 559
Owen, C. J., Bruno, R., Livi, S., et al. 2020, A&A, 642, A16
Palmerio, E., Carcaboso, F., Khoo, L. Y., et al. 2024, ApJ, 963, 108
Palmerio, E., Kilpua, E. K. J., Witasse, O., et al. 2021, SpWea, 19, e2020SW002654
Palmerio, E., Lee, C. O., Mays, M. L., et al. 2022, SpWea, 20, e2021SW002993
Patsourakos, S., & Vourlidas, A. 2012, SoPh, 281, 187
Pesnell, W. D., Thompson, B. J., & Chamberlin, P. C. 2012, SoPh, 275, 3
Pinto, M., Sanchez-Cano, B., Moissl, R., et al. 2022, SSRv, 218, 54
Ramstad, R., Holmstrom, M., Futaana, Y., et al. 2018, GeoRL, 45, 7306
Reames, D. V., Barbier, L. M., & Ng, C. K. 1996, ApJ, 466, 473
Reames, D. V., Ng, C. K., & Tylka, A. J. 2013, SoPh, 285, 233
Reiner, M. J., Kaiser, M. L., Fainberg, J., et al. 1998, GeoRL, 25, 2493
Reiner, M. J., Kaiser, M. L., Karlický, M., et al. 2001, SoPh, 204, 121
Richardson, I. G., & Cane, H. V. 1993, JGR, 98, 15295
Richardson, I. G., & Cane, H. V. 1996, JGR, 101, 27521
Richardson, I. G., von Rosenvinge, T. T., Cane, H. V., et al. 2014, SoPh, 289, 3059
Rochus, P., Auchere, F., Berghmans, D., et al. 2020, A&A, 642, A8
Rodríguez-García, L., Gómez-Herrero, R., Zouganelis, I., et al. 2021, A&A, 653, A137
Rodríguez-Pacheco, J., Wimmer-Schweingruber, R. F., Mason, G. M., et al. 2020, A&A, 642, A7

Sánchez-Cano, B., Witasse, O., Knutsen, E. W., et al. 2023, SpWea, 21, e2023SW003540
Sánchez–Cano, B., Blelly, P., Lester, M., et al. 2019, JGRA, 124, 4556
Stone, E. C., Frandsen, A. M., Mewaldt, R. A., et al. 1998, SSRv, 86, 1
Thernisien, A., Vourlidas, A., & Howard, R. A. 2009, SoPh, 256, 111
Thernisien, A. F. R., Howard, R. A., & Vourlidas, A. 2006, ApJ, 652, 763
Thompson, W. T. 2006, A&A, 449, 791
Torsti, J., Valtonen, E., Lumme, M., et al. 1995, SoPh, 162, 505
Verbeke, C., Mays, M. L., Kay, C., et al. 2022, AdSpR, 72, 5243
von Rosenvinge, T. T., Richardson, I. G., Reames, D. V., et al. 2009, SoPh, 256, 443
Wei, W., Lee, C. O., Lynch, B. J., et al. 2023, in AGU Fall Meeting, SH51C–2625
Wibberenz, G., & Cane, H. V. 2006, ApJ, 650, 1199
Wild, J. P. 1950, AuSRA, 3, 541
Xie St., H., Cyr, O. C., Mäkelä, P., & Gopalswamy, N. 2019, JGRA, 124, 6384
Zeitlin, C., Hassler, D. M., Guo, J., et al. 2018, GeoRL, 45, 5845